WILEY-VCH

Exhaled aerosols and saliva droplets measured in time and 3D space: Quantification of pathogens flow rate applied to SARS-CoV-2

*Adrian Roth[1], Mehdi Stiti[1], David Frantz[1], Andrew Corber[2], and Edouard Berrocal[1]**

1) Department of Physics, Faculty of Engineering, Lund University, Lund, Sweden
2) Aerospace Research Centre, National Research Council of Canada, Ottawa, Canada
E-mail: edouard.berrocal@forbrf.lth.se

Keywords: COVID-19, virus spreading, saliva particle sizing, 3D high-speed imaging

SARS-CoV-2 and its ever-emerging variants, are spread from host-to-host via expelled respiratory aerosols and saliva droplets. Knowing the number of virions which are exhaled by a person requires precise measurements of the size, count, velocity and trajectory of the virus-laden particles that are ejected directly from the mouth. These measurements are achieved in 3D, at 15 000 images/second, and are applied when speaking, yelling, and coughing. In this study 33 events have been analysed by post-processing ~500 000 images. Using these data, the flow rate of SARS-CoV-2 virions have been evaluated. At high concentrations, 10^7 virions/mL, it is found that 136 to 231 virions are ejected during a single cough, where the virion flow rate peak is capable of reaching 32 virions within a millisecond. This peak can reach tens of virions/ms when yelling, but reduced to only a few virions/ms when speaking. At medium concentrations, ~10^5 virions/mL, those results are hundreds of times lower. The total number of virions that are ejected when yelling at 110 dB, instead of speaking at 85 dB, increases by two to three fold. From the measured data analysed in this article, the flow rate of other diseases such as influenza, tuberculosis or measles, can also be estimated. As these data are openly accessible, they can be used by modellers for the simulation of saliva droplet transport and evaporation, allowing to further advance our understanding of airborne pathogen transmission.

1. INTRODUCTION

It is now well established that surface transmission is not the primary pathway by which SARS-CoV-2 is spread.[1-4] The current thinking is that air transport is the more direct and rapid route. The airborne transmission is defined as particles emitted by a person - via breathing, speaking, coughing and sneezing - carried through the air and being inhaled by another person. Since the concentration of suspended particles reduces significantly away from their emission, the probability of their transmission is directly related to the distance in between two persons. Medical researchers usually divide the particles found in human respiratory emissions into two categories: “aerosols”, which are in the air for long periods of time, and “droplets” which reside in the air for shorter periods prior to falling to the ground.[5] There is no size that strictly separates the two, however 5 µm is commonly used and this value has been adopted by the Centre for Disease Control (CDC) as well as the World Health Organization (WHO). In this article, the liquid particles that are directly ejected from the mouth are divided into four categories: The *aerosols* below 5 µm; the *large aerosols* between 5 and 20 µm; the *droplets* between 20 and 100 µm; and the *large droplets* above 100 µm. This categorization is described and illustrated in **Figure 1**a. Depending on their initial size and their liquid/solid content, the air transport of the emitted particles remains complex due to their evaporation over time. In an earlier study of saliva droplet evaporation,[6] pure water was considered. As the liquid properties of saliva are more complex than pure water, a binary mixture of water and NaCl salt must instead be considered.[7-9] The experimental validation of such numerical models can be achieved using an acoustic levitator, in which saliva droplets are levitated at a fixed location allowing them to be imaged over time. By means of a reliable validated model,[9] it has recently been demonstrated that the water content of a

saliva droplet with an initial diameter as large as 21 µm evaporates in less than 2 seconds, forming a residual solid aerosol 5 µm in diameter. This rapid transition depends on air temperature and humidity, with the shrinkage resulting in a particle that is on average 23.5% of its initial diameter. Other simulation results from this model,[9] are shown in Figure 1b. A saliva particle with an initial diameter of 20 µm becomes a 4.7 µm solid residue within less than a second, assuming the air has a relative humidity of RH = 60% and an ambient temperature of T_{amb} = 20°C. This dry solid particle remains at the same vertical position after travelling 1.2 meters away from its emission source when assuming a cough with an initial air speed of 10 m/s. This demonstrates that ejected *large aerosols*, ranging in initial diameters between 5 - 20 µm, evaporate very rapidly and become solid particles with final diameters of 1.2 - 4.7 µm. Those small solid particles can remain suspended in the air for several hours, leading to a high probability of airborne transmission of the virus to another host. Once inhaled, they can then penetrate deeply into the lungs and deposit in the alveolar lumen.

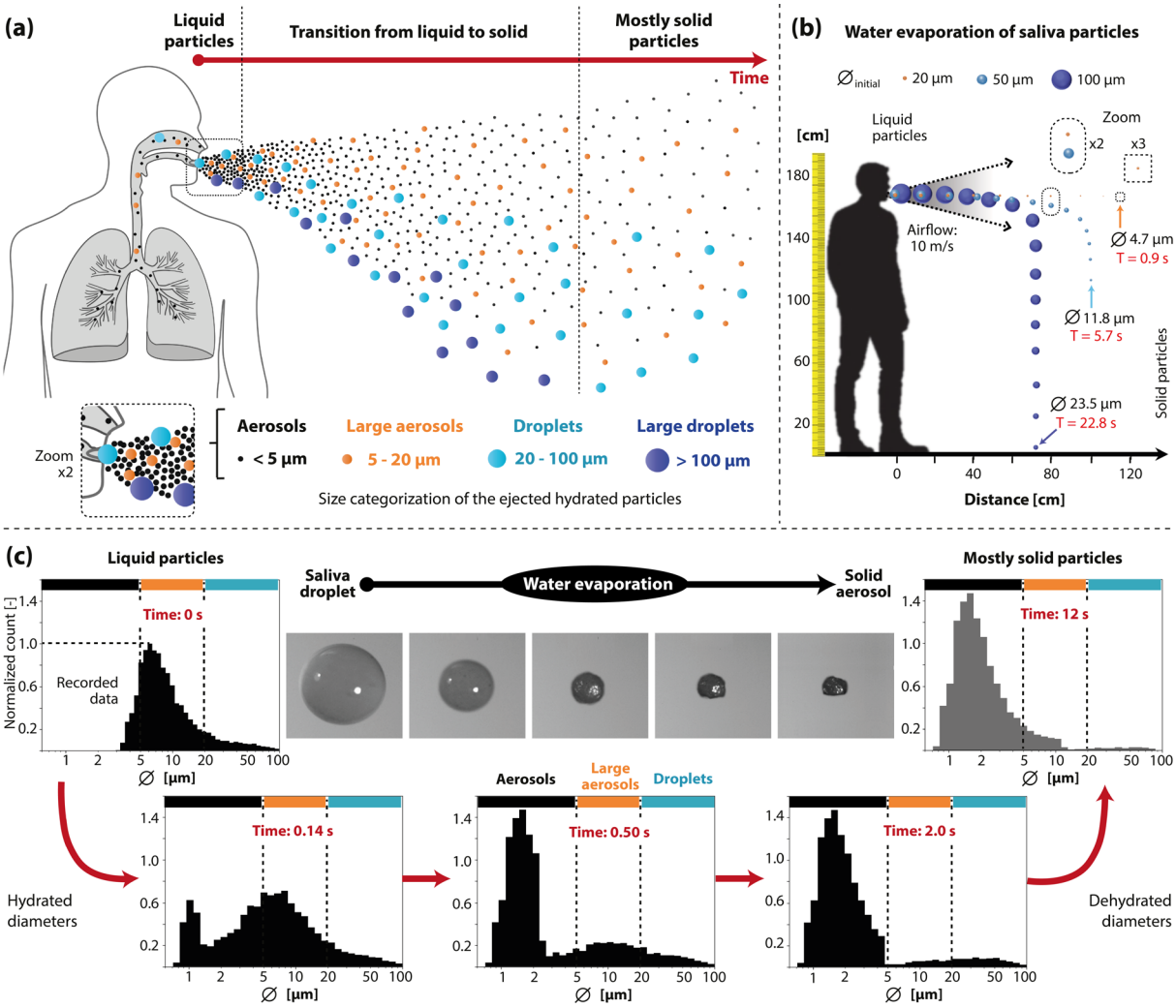

FIGURE 1 (a) Categorization of exhaled particles as a function of their initial size. The ejected particles transit from liquid to solid overtime due to rapid water evaporation. Simulated results of this effect, combined with the particle propagation induced by an airflow velocity of 10 m/s during a cough, is shown in (b). Those simulations are generated using the model developed in Ref. [9], assuming initial particle sizes of 20, 50 and 100 µm exhausted in air with a relative humidity of RH = 60% and an ambient temperature of T_{amb} = 20°C. (c) Size distribution of ejected particles measured in this study between 3.2 and 100 µm, become a distribution of solid aerosols between 740 nm and 100 µm, after evaporation. Such transition is experimentally shown for a single levitated saliva droplet, allowing the validation of the numerical model [9] used here to deduce the particle size distribution over time. Here, a high relative humidity of RH = 80% as been assumed, to consider the high humidity of the exhaled air flow. Despite this high RH, the drying of particles below 20 µm remains fast, below 2 seconds at T_{amb} = 22°C.

As originally mentioned by Duguid in 1934 in Ref. [10] and recently summarised in Ref. [11], saliva droplets 100 µm in diameter represent the largest particles that can remain in the air for more than 5 s and still propagate at distances of more than 1 m from the host. Thus, such wide exhaled particles can still be inhaled by a second person positioned at close distance. Particles with an initial diameter of more than 100 µm, belong to the category of *large droplets*, and quickly fall to the ground leading to virus transmission via fomite rather than airborne pathways.
Figure 1b,c show the state and position of saliva particles a few seconds after exhalation until they become residues that are fully solid. During and after this liquid to solid phase transition, particles can be further transported over several meters [12] and are subjected to the mixing between the exhaled gases and surrounding flows.[13] The complexity of this turbulent multiphase flow system, and the small size of the resulting particles, makes experimental observations of the complete process a challenge. This is an issue, since accurate and predictable 3D computations of saliva particle transport, requires detailed information regarding their initial size, velocity, and position, near the mouth of a subject. Those boundary conditions must be well defined prior to tracking their transport and evolution in time and space.[14-17] Unfortunately, detailed and complete sets of data are difficult to collect at the source given the speed of the flows, the broad range of droplet/aerosol sizes, and the large areas/volumes that need to be surveyed. These measurements are the main focus of this article.

Determining the global size distribution of the ejected saliva particles is laborious due to its wide range, which spans from a few microns to several millimetres. Additionally, the particle population will change in space and time due to the rapid evaporation of the droplet water content, further exacerbating the task. These complications greatly limit the effectiveness of historical diagnostic tools such as the Aerodynamic Particle Sizer (APS),[18-20] which sizes particles from 0.5 to 20 µm in diameter, and returns time-averaged sizing information from a singular area in space. This tool collects a sample using a mechanical probe, whereby aerosols are guided into the analyser. In the time needed to transport the sample into the measurement volume, the water in the saliva droplets will evaporate leading to solid aerosols. Since the approach cannot capture temporally or spatially resolved information, the results obtained offer limited insight into the realistic dynamics of these flow fields.

To acquire spatially resolved measurements of droplet size, imaging-based techniques must be employed. High-resolution white light shadowgraphy is a popular approach in the field of spray research where droplets as small as ~5 µm can be imaged using a long-distance microscope objective.[21] Imaging at such a high spatial resolution comes at the cost of a small viewable area, typically in the range of a few square millimetres. While such measurements can be achieved easily using a monodispersed droplet generator, they are hard to apply in the case of human speech, which generates droplets in a transient and uncontrolled manner, both in space and time.

Some of the issues described above, have been addressed by a technique called Interferometric Laser Imaging for Droplet Sizing (ILIDS).[22] In this approach, droplets are illuminated with a laser sheet and imaged out-of-focus (at ~70° detection angle) to generate interference fringes whose frequencies are related to droplet diameter. This configuration allows the imaged area to be extended to a few cubic centimetres. While ILIDS is ideally suited for sizing transparent spherical droplets,[23] it becomes challenging to implement in situations with non-spherical solid particles. This is perhaps why only a couple of applications of ILIDS have been used in the study of expelled saliva droplets.[24,25] The need for a larger depth-of-field, while preserving high spatial resolution, has recently motivated the use of Digital Inline Holography (DIH).[26,27] A major benefit of DIH is its ability to generate 3D reconstructions of the particles, allowing them to be categorized according to their respective shape. Although DIH and ILIDS present interesting sizing features, they remain limited to small measurement areas. Since they do not cover the total area of what is naturally ejected from the mouth, only part of the flow field produced by an exhalation event is spatially resolved by those imaging techniques.
To visualize and characterize exhaled airflows, three common approaches have been applied: Schlieren, thermal radiation detection, and Particle Image Velocimetry (PIV). Schlieren[28] is a photographic technique that produces shadowgrams of the density changes throughout the flow field. The technique has been used at a frame rate of several kilohertz to analyse the exhaled air front,[29,30] as

well as to assess air-flow leakages around facemasks.[31] The approach is based on the detection of thermal radiation,[32] and uses near-infrared cameras to observe the warm exhaled airflows.[33] The third method, PIV, relies on seeding the surrounding air with particles which are tracked over time. A recent study used PIV to show how different transport mechanisms are responsible for the propagation of air over short and long distances for speaking and breathing scenarios.[34] However, this approach suffers from two limiting factors. Firstly, PIV measurements have difficulty differentiating between the particles produced by the subject and the seeds introduced by the researchers, and secondly lack any 3D tracking information due to the use of a thin laser sheet.

To detect and visualize the exhaled particles, various light-scattering based approaches are employed. White light illumination strategies employing powerful LEDs, have been used in conjunction with various source/detector configurations to image saliva droplets. Backscattering detection experiments have shown that the large droplets produced from a sneeze can propagate distances of over 6 m.[35] Side-scattering detections have been applied to the study of facemasks in order to determine their blocking efficiency.[36] Semi-forward scattering detection schemes have also been employed for analyzing singing events.[37] Despite their benefits, powerful white light sources are not bright enough for the observation of the small and fast-moving particles near the mouth. By using an intense laser sheet instead, micrometric aerosols can be detected over a 2D area. This was demonstrated for the first time in 1979, where aerosols with diameters less than 1 µm were imaged using a TV camera as the detector.[38] This early development paved the way for nearly four decades of PIV measurements.[39] It is no surprise then, that modern camera phones can also detect the light scattered by saliva droplets illuminated via a laser sheet.[40,41] Data have been collected this way by taking images long after ejection, and have been used for assessing the performance of protective face masks[42]. The collection of relevant quantitative data near the mouth requires much faster recording rates, [43] typically in the range of 10-20 kHz, with an exposure time between 10-100 µs. Camera phones are simply not up to this task as they lack the required frame rate and shutter speed.

In this work, we present an optimized imaging tool for the complete characterization of the liquid particle flows produced by human exhalations. Those respiratory droplets are measured near the mouth and are categorized into four groups, as shown in the lower portion of Figure 1a. Thus, hydrated diameters are directly measured in this study, and the corresponding dehydrated diameters have been calculated. The system, detailed in **Figure 2**a and in **Movie S1**, operates at high-speed, reaching an image recording rate of 15 kHz. The semi-forward detection strategy employed here, at 52° detection angle, results in light intensity signals that are up to 30 times higher than a conventional perpendicular detection angle. This configuration allows sizing of the ejected saliva particles down to 3.2 µm, which become 740 nm solid aerosols in less than 0.5 seconds. As the ejected particles are detected directly when exiting the mouth, many of them belong to the categories of *large aerosols* and *droplets*, prior to evaporation. A measured size distribution of saliva particles, transiting into solid particles is shown Figure 1c. With the current laser illumination and camera system, the setup is capable of accurately measuring droplets up to 100 µm, particle speeds up to 56 m/s, and 3D trajectories over a distance of either 15 mm or 120 mm. Three-dimensional temporally resolved measurements were performed at ~10 mm from the lips of a person speaking, yelling and coughing. Before any recordings were taken, particles in the air were removed. Additionally, it was verified that the cameras were not detecting any signal prior to the opening of the mouth of the subject. For the speaking and yelling cases the sentence "*Protect better against COVID*" was used since it contains several explosive syllables. A sound level meter was placed 15 cm from the subject in order to quantify the maximum decibel level of each event. A total data set of 33 events (7 speaking, 7 yelling and 19 coughing) have been obtained from three persons: Subjects #1 a 42 years old man, Subject #2 a 27 years old man and Subject #3 a 30 years old man. From those measurements, the flow rates and total number of exhaled SARS-CoV-2 virions ejected over time and space have been deduced. The presented data are openly accessible and free to download, from Ref. [44] providing modelers with a realistic and complete set of input data. The "Results" section presents the experimental results for individual events related to Subject #1, while the data collected for Subjects #2 and #3 are shown in the supplementary information. Finally, the quantification of SARS-CoV-2 virions flow rate is compared for all three subjects and for each exhalation case. Those findings are discussed in section 3.

2. METHODS AND RESULTS

2.1. Instantaneous sizing and velocity of exhaled particles

The illumination strategy used in this study, detailed in Figure 2a and in **Movie S1**, combines two powerful CW laser beams (λ = 450 nm and 532 nm) with a dichroic mirror to obtain a total laser power of 9 W. This commanding light intensity enables high detection sensitivity to small particles, even within a relatively large 3D illumination volume. The recombined beams are shaped to form a homogeneous top-hat intensity profile that is 15 mm thick and 120 mm high. Using this deep planar illumination instead of a thin light sheet, allows the saliva droplets to be tracked through a well-defined volume, rather than just a 2D plane. As this volume was positioned at only ~10 mm from the subject's lips, it ensured that all droplets ejected within ±72° half-angle were illuminated. The imaging system consists of two cameras (high-speed cameras Phantom VEO 710) operating simultaneously at 15 kHz and with an exposure time of 50 µs. This high-speed stereoscopic arrangement enables a 3D triangulation, which works with a particle tracking velocimetry algorithm to calculate individual droplet trajectories and velocities within the illuminated volume. The procedure allowing the 3D tracking of the saliva droplets is detailed in Figure 9. The cameras are positioned at an angle of 52° from the incident laser beam direction, optimizing both the 3D triangulation and the strength of the detected scattered light.
The light intensity scattered by a droplet of more than twice the size of the illumination wavelength is related to its surface area and thus, its diameter.[45,46] This signal was detected between 48° and 56° due to the collection angle defined by the position and dimensions of the objective from Cam.2. This recorded intensity was correlated to the droplet diameter using a curve calculated by the Lorenz-Mie theory. The theoretical curve was calibrated using high-resolution shadowgraph images recorded from Cam.1. This allowed us to obtain the diameter of each ejected saliva droplet from the intensity signal detected by Cam.2. The generation of this calibration curve is detailed in Section 5. During the experimental protocol a person was asked to speak, yell, or cough, and each event was synchronized with both cameras. All the experiments were conducted under a relative humidity between 40% and 50% and an ambient temperature of T_{amb} = 22°C.

The 3D trajectory and velocity of the ejected micrometric saliva droplets, along a range of 10-25 mm from the mouth, are shown in Figure 2b. While those droplets are transported within the exhaled primary airflow direction, a more rapid and linear transport is observed when coughing than when speaking. It can also be seen that the droplets cover a larger area when speaking and yelling in comparison to coughing. The trajectory of the droplets over time, during the coughing event, given in Figure 2b, is provided in the first part of **Movie S2**. The velocity is the highest for the coughing events, reaching speeds over 25 m/s, where a straighter forward directionality is obtained. Similar 3D droplet tracking data when considering other events are given in **Figure S1**, **S2** and **S3** from Subject #1, #2 and #3 respectively.

In Figure 2c the count, velocity, and size of the ejected respiratory droplets and aerosols for each event have been quantified over time. For the speaking and yelling scenarios the correlations between these parameters can be observed for each individual word that was enunciated. It is thus possible to observe a sudden droplet emission when the letters "P", "B" and "V" in the words "Protect", "Better" and "COVID" are spoken. These letters are explosive syllables,[43] generating a large number of droplets that are expelled at higher speed than the other letters. By examining the averaged droplet velocity over the full image, the highest velocity occurs when the letter "P" is spoken, corresponding to speeds of 4.2 m/s for speaking and 6 m/s for yelling. When coughing, the droplet velocities are even higher, with spatially averaged speeds exceeding 8.5 m/s at the start of a cough. Exploiting the fact that each event is temporally resolved, droplet flow rates can be obtained. From this example, a maximum of 120 and 460 particles are ejected considering a temporal window of 20 ms when speaking and yelling respectively. When coughing, a maximum of 450 particles are ejected in only 5 ms. This leads to a flow rate reaching 90 particles/ms when coughing versus 23 and 6 particles/ms when yelling and speaking respectively. This quantification justifies the practice recommended by numerous health organizations who prescribe coughing into a sleeve to efficiently avoid the expulsion of a large number of virus-laden droplets.

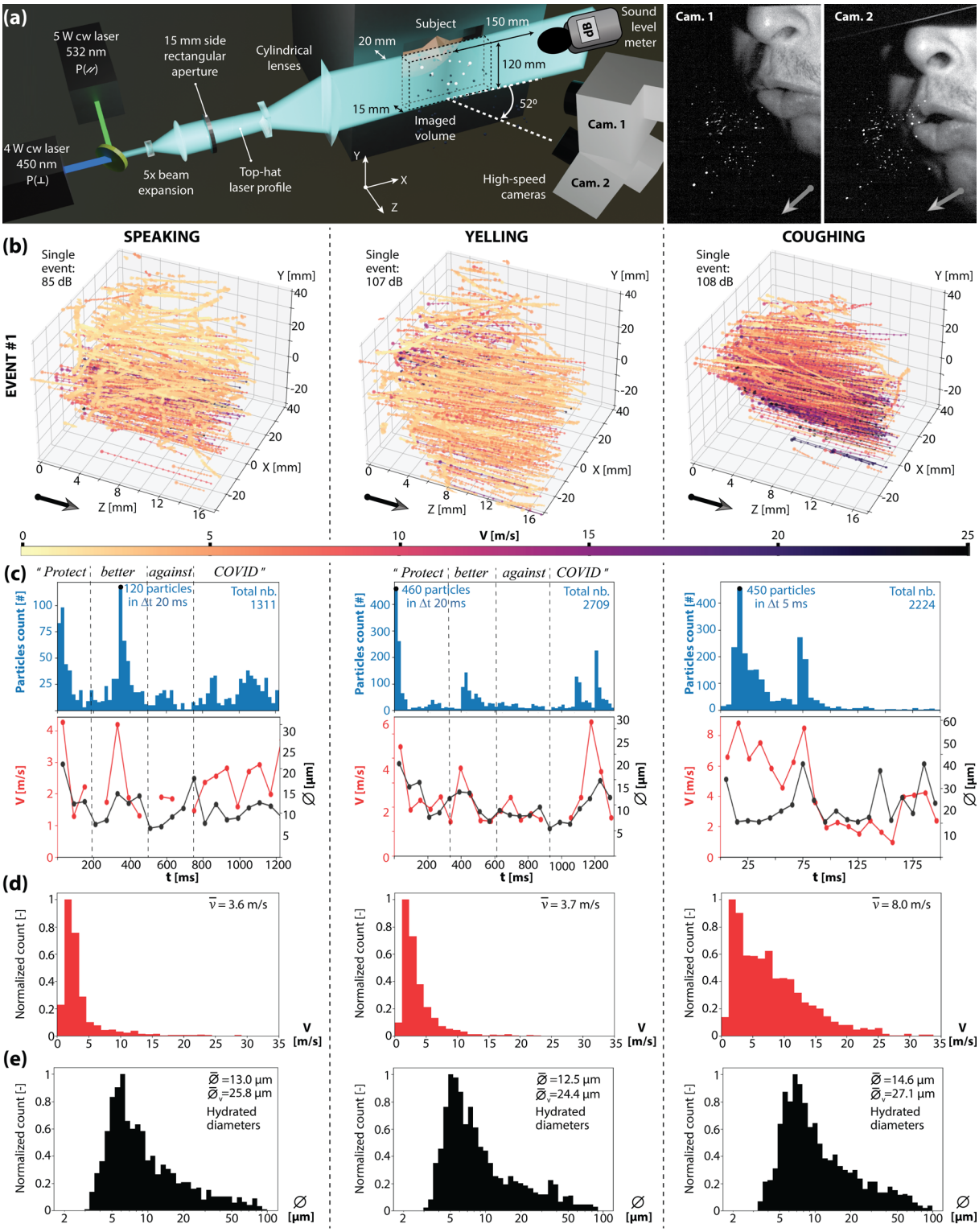

FIGURE 2 Simultaneous counting, sizing and 3D tracking of expelled saliva droplets from Subject #1, for speaking, yelling and coughing. (a) Description of the optical arrangement for measuring both the 3D trajectory and the size of saliva droplets at 15 kHz frame rate. Two CW laser beams are shaped to form an illumination volume of 15 mm thick by 120 mm high. The light scattered by the exhaled droplets was detected in the semi-forward scattering direction (52°) to optimize 30 times the detection sensitivity. An example of the raw images collected by this stereoscopic arrangement is given on the right. (b) Results of the 3D droplet trajectories obtained for speaking at 85 dB, yelling at 107 dB, and coughing at 108 dB, respectively. (c) Temporal evolution of the instantaneous droplet counting, velocity, and diameter shown for each respective event. For the speech cases, the time scale is divided as a function of each word being pronounced. The normalized histogram distributions of the resulting velocity and droplet size are shown in (d) and (e) respectively. Data have been cumulated over each respective event. The mean value is indicated in the upper right corner of each distribution.

The histograms of the velocity distribution are given in Figure 2D, showing a slight broadening when yelling in comparison with speaking, while a much larger one occurs when coughing. The highest velocities are recorded when coughing, with a mean velocity of $\bar{v}$ = 8.0 m/s over the entire event. When yelling the mean droplet velocity was found to be around half that of coughing, $\bar{v}$ = 3.7 m/s, and slightly higher than for speaking, where $\bar{v}$ = 3.6 m/s.
The histograms of the particle size distribution, given in Figure 2e, indicate that the mean geometrical diameter is slightly higher for coughing, where $\bar{\emptyset}$ = 14.6 µm, in comparison to the speaking and yelling cases, where $\bar{\emptyset}$ ~ 13 µm. The volumetric mean diameter, $\bar{\emptyset}_v$, is also indicated in the figures. The differences between a geometrical and a volumetric mean diameter are impacted by the presence of a few large diameter droplets. In this study, the maximum particle size measured is 100 µm. Larger droplets are not considered in the calculation of the volumetric mean diameter. Thus, the range between 50 and 100 µm is mostly impacting the variations between $\bar{\emptyset}$ and $\bar{\emptyset}_v$. The volumetric average diameters are found to be twice as large as the standard mean diameter, and are 25.8 µm for speaking, 24.4 µm for yelling, and 27.1 µm for coughing. Despite their low number, large droplets have a much higher probability of containing virions due to the volumetric dependence. Note that the droplet diameter distribution resolved in time during the coughing event shown in Figure 2e, is provided in the second part of Movie S2.

2.2. Averaged sizing and velocity data of exhaled particles

Statistical characteristics of the ejected saliva droplets, are given in **Figure 3**. Data from three speaking events, three yelling events, and six coughing events have been considered and averaged. While those averaged results are related to Subject #1 in this subsection, similar data are given for Subject #2 and Subject #3 in SI Appendix **Figure S5** and **S6** respectively.
In Figure 3a the histograms of the particle count, mean velocity, and mean diameter are shown and can be used to compare events. It shows the total particle count per event varies between 1200 to 2000 when the sentence "*Protect better against COVID*" is spoken normally, but increases substantially to between 1500 to 2700, when yelling it. For the case of a cough, the number of detected droplets ranges from 700 to 3000.

To gain a statistical representation of the data, accumulated and normalized histograms are shown for the droplet velocity and diameter. The highest mean velocities, $\bar{v}$, for speaking, yelling, and coughing, are given in Figure 3b and are 3.4 m/s, 4.2 m/s, and 7.2 m/s, respectively. In the speaking and yelling cases an increase in velocity is correlated with an increase in sound level. The sound level was ~86 dB for speaking and ~107 dB for shouting. For the coughing case, the velocity increase is attributed to the mouth being more closed combined with an increase in airflow. Even though the averaged particle velocity is found to be significantly lower when yelling than when coughing, we observe the fastest particle reached 42 m/s when yelling and 34 m/s when coughing. Similar results were seen for the Subject #2 and Subject #3 yelling cases, with particles achieving speeds above 40 m/s. Those few droplets that reach this high velocity travel a longer distance, increasing the risk of virus transmission between two people standing several meters away from each other.

The size distributions given in Figure 3c appear to be independent of the exhalation type, with a mean diameter falling around ~13 µm from Subject #1 and ~9.5 µm from Subject #3 (see Figure S3c). However, for Subject #2 (see Figure S2c), larger droplets were observed for coughing, with $\bar{\emptyset}$ = 15.6 µm, and smaller droplets for yelling, with $\bar{\emptyset}$ = 7.5 µm.

The size distribution of the particles, after 12 seconds of evaporation, is shown in Figure 3d. Those results are deduced after water evaporation, as detailed in Figure 1c. A large majority of the particles are now < 5 µm, belonging to the aerosol category. The resulting average size $\bar{\emptyset}$ is found to be in between 2 and 4 µm, for all emission scenarios and all subjects.

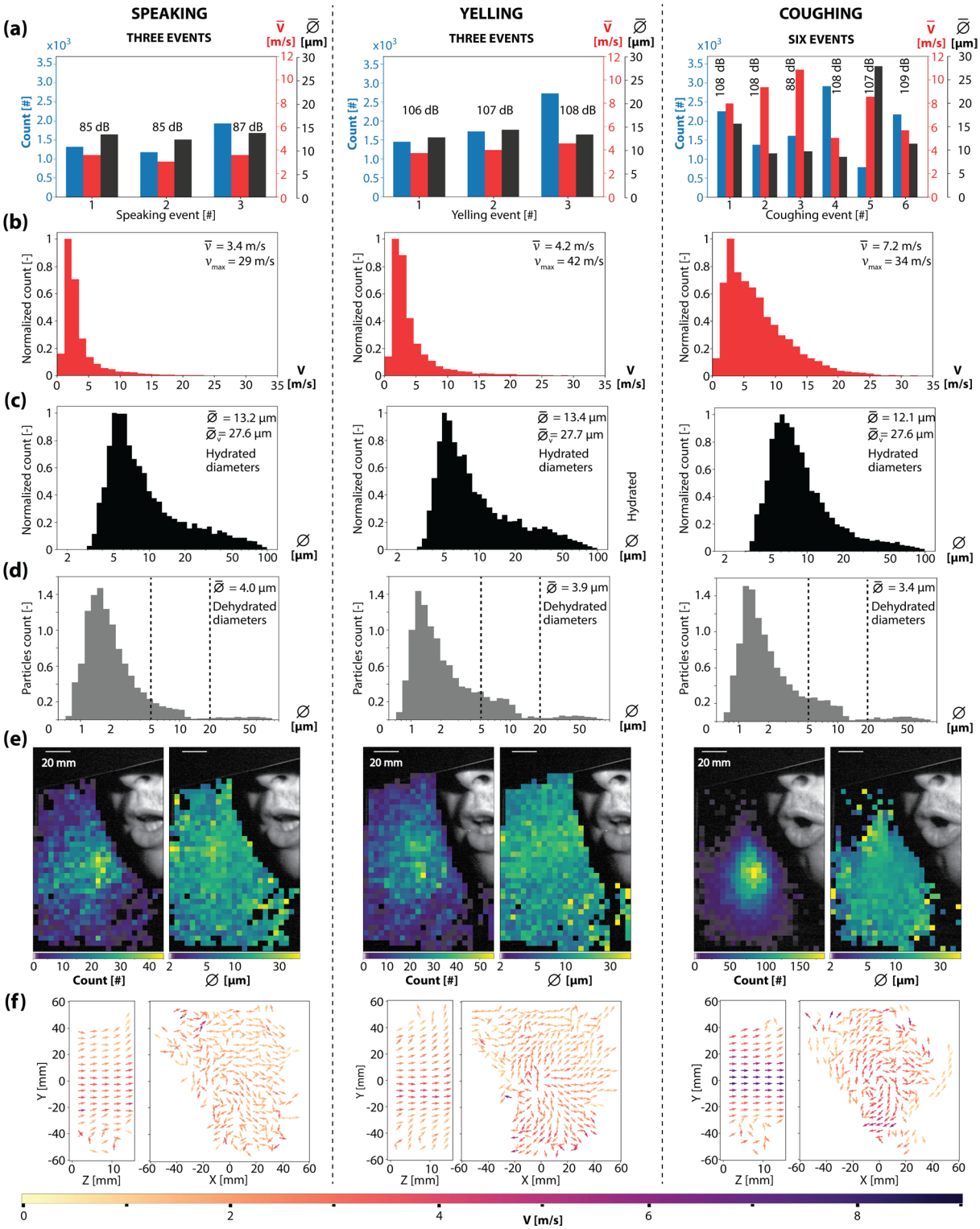

FIGURE 3 Accumulated counting, sizing and velocimetry data for the saliva droplets ejected from Subject #1. (a) Total count, mean droplet diameter, and maximum velocity obtained from three speaking events, three yelling events, and six coughing events. The corresponding sound level for each event is also indicated. (b) Droplet velocity $\bar{v}$ accumulated and averaged over all events for yelling, speaking, and coughing, respectively. The overall mean value is indicated in the upper right corner of each histogram. (c) shows the particle size histograms of the ejected liquid aerosols and droplets. The averaged diameter of the distribution $\overline{\emptyset}$ and the diameter the averaged volume $\overline{\emptyset}_v$ are both indicated. (d) shows the particle size histograms formed 12 seconds after water evaporation. (e) Spatial distribution and the corresponding size of the ejected droplets. Data are binned into 16 mm^2 areas. It is observed that for the coughing case the position of saliva droplets is localized into a smaller and well-defined area. f) 2D maps of the averaged velocity of the saliva droplets viewed either from the side (YZ axis) or from the front (XY axis) of Subject #1.

The counting and sizing averages, resolved in 2D space, are presented in Figure 3e. The largest number of particles is found in the centre of the emitted population for the case of coughing. More localized droplet emissions are observed when yelling in comparison with speaking, from the two other subjects (see Figure S5e,S6e). Interestingly, no correlation is observed between the droplet size and position, with droplets of all sizes distributed throughout the sample space. This supports the theory that the distributions of saliva droplets are randomized in size and space for all types of exhalations.

The 2D maps of accumulated and averaged velocity vectors are presented in Figure 3f. The maximum velocity was found to be in the centre of the YZ views. The velocity differences observed between the speech and cough scenarios are related to the differences in both the exhaled airflow and the mouth opening as shown in the pictures. We observe that when coughing the mouth opening appears slightly smaller in comparison to the one observed when speaking or yelling.

2.3. Deceleration of coughed particles

During the first few milliseconds after their expulsion from the mouth, the respiratory droplets decelerate due to the drag forces acting on them. This deceleration depends on their size and the speed of the surrounding airflow. In the context of a transient episode, the local airflow is highly dependent on the time and distance from the start of the event. The analysis of coughed particles[14] propagating their first 20 ms, requires a tracking along a distance over 10 to 20 cm from the mouth. In the previous section, the particles were only tracked over 15 mm, corresponding to the width of the vertical planar illumination. By positioning this illumination horizontally in front of the mouth, as shown in **Figure 4**a, a length of 120 mm ahead from the mouth is achieved. This imaging configuration is the one used in the subsection analysing the deceleration and trajectory of ejected saliva particles during a cough.

The trajectories and speeds of the particles ejected by Subject #1, are tracked in 2D in Figure 4b. The results of each particle size category, defined in Figure 1, are also given. As expected, the speeds are mainly higher close to the mouth and successively decrease as particles travel forward. When ejected, those particles are transported via the intense air flow of the cough. As the air plume expands and mixes with the ambient air, the average air speed decreases. Consequently, the particles are subject to a drag force depending on their speed relative to the surrounding air. When traveling towards the sides of jet, they escape the central air plume and experience a greater deceleration. These effects are especially noticeable for the *aerosols* ($Ø < 5$ µm). Due to their tiny mass (momentum), their velocities are easily influenced, and faithfully follow the local airflow. This causes more erratic movements for the aerosols in comparison to larger particles.
The particles that are tracked by both cameras allows the visualization of their speed and displacement in 3D, given in Figure 4c. A selection of 15 tracked particles, spanning a wide variety of initial speeds, trajectories, and size, are shown in Figure 4d. Their final position and travel time are also indicated. These selected particles are ordered by their size and grouped into two categories: The *large aerosols* ($5 < Ø < 20$ µm) numbered from (1) to (7), and the *droplets* ($20 < Ø < 100$ µm) numbered from (8) to (15).

To analyse in detail the deceleration of those particles, their speeds are plotted as a function of time in Figure 4e. For the *droplets*, an exponential decay from their initial velocity is observed. This decrease in velocity is mainly related to the drag force effect, with different trajectories resulting in varying decay rates. For example, particle (14) has a high decay rate, from 14 m/s to 5 m/s in 15.9 ms, while particle (12) has a slower decay, from 12 m/s to 5.2 m/s in 12.7 ms. In contrast, some droplets do not follow this expected deceleration: particle (9) experiences a sharp velocity increase of ~2 m/s at 3 ms, and particle (13) has a speed plateau at ~11 m/s between 3 and 7 ms. It is notable, from Figure 4d, that those two droplets are ejected from the same location and follow a similar track in the middle of the cough air flow. This behaviour of transportation indicates the presence of turbulence leading to a strong non-monotonic airflow in the centre of the cough.

In contrast to the speed of the *droplets*, the speeds of the *large aerosols* have no common trend. Those particles have a large spread of initial speeds, as well as various speed fluctuations leading to various winding paths through the central region. The presence of the strong non-monotonic airflow, present during this event, has direct impacts on the velocity and directionality of the low mass particles. For example, particle (5) moves diagonally across the central region of the flow, with a speed fluctuating between 3 m/s and 12 m/s, including five local maxima and a randomized propagation path. Particle (4) has a twitching forward-moving path with a speed between 10 m/s and 4 m/s and three local minima.

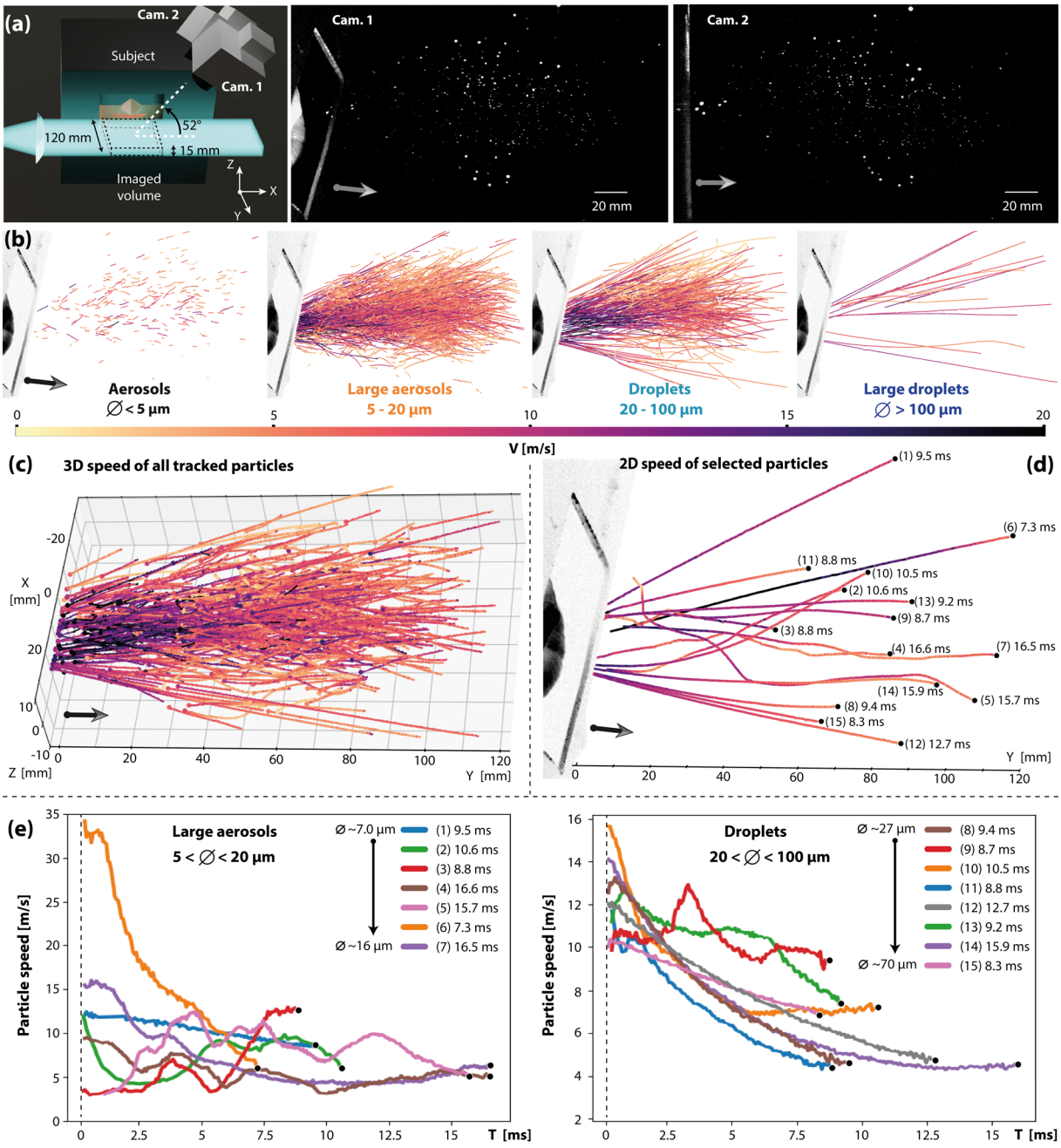

FIGURE 4 (a) Imaging configuration with horizontal light sheet and example raw data which enable 120 mm of tracking in a 15 mm thick volume. (b) Speeds and paths of particles in 2D from a single coughing event, separated into the size categories: aerosols, large aerosols, droplets, and large droplets. (c) Speeds and paths of particles in 3D from a single coughing event. (d) 15 selected particle paths and speeds in 2D. (e) Particle speed over time for the 15 selected particles, separated by size category: *large aerosols* (left) and *droplets* (right).

On the contrary, particle (1) has a straight trajectory away from the central region and does indeed, exhibit more monotonous deceleration. Particle (6) also stands out with a significantly higher initial speed of ~34 m/s, and a rapid monotone deceleration despite traveling close to the central region. The high-speed makes the associated drag force dominate the forces on the particle and ensures that the particle quickly leaves any turbulent flows along its path, giving a straight trajectory.
These 15 particles represent distinct trajectory modes: (A) Particles traveling in straight trajectories, with a monotone exponential-like deceleration. (B) Particles traveling in wiggling paths with fluctuating speeds involving various positive accelerations. A third mode (C), defined as intermediate corresponds to trajectories that are neither straight nor wiggly but travel in smooth bent trajectories with a non-monotone varying deceleration.
As seen in Figure 4b, most high mass particles which mainly involve the droplets, travel in mode (A). A few large aerosols, such as particles (1) and (6), also travel in this mode. This is due to their high initial speed and angle of trajectory, transporting them away from the centre of the air flow. Thus, particles of mode (A) have one of the following dominating characteristics: High momentum and weak or constant aerodynamic forces.
Conversely, most low mass particles mainly involving the aerosols, travel in mode (B). These particles are subject to forces that are strong enough to change their velocity and transport direction. Note that their wiggling path and their small size make those particles hard to track experimentally. Some droplets travelling in the centre of the air flow, such as particle (9), also move in this mode, as they are subject to strong changing forces. As a result, mode (B) particles have one of two dominating characteristics: Low momentum and strong varying aerodynamic forces.
Finally, some particles, such as (10) and (13), are travelling in mode (C). They have a moderate initial momentum (13) or are subject to moderately strong forces (10). Their exponential deceleration is not monotone like in mode (A), and they do not accelerate like in mode (B). It is expected that once particles leave an area of strong varying aerodynamic forces, or experience a gain or loss in momentum, may transition between modes (A) and (B), corresponding to mode (C).

3. DISCUSSION

3.1. SARS-CoV-2 concentrations in saliva

The optical setup with a 15 kHz recording frame rate, has allowed for the accurate observation of particles count and size variability in time, for different exhalation events. From those experimental data, the volume of ejected saliva can be calculated, as demonstrated in **Figure 5** and shown by the green curve in A. By knowing the viral load (defined as C in virions/mL) contained in the saliva of the infected person, the evaluation of the number of virions emitted during an event can be deduced. Recent studies, published in articles,[47-51] indicate the concentration of SARS-CoV-2 virions in the saliva of infected people. Those results, gathered in Figure 5b, correspond to the 5 first days after the perception of initial symptoms. The data represent a total of 75 infected persons, where the measurements range from 10^3 to 10^9 virions/mL, and with a median concentration of approximately 10^6 virions/mL. The virion concentration varies greatly between people, as well as over the time after which symptoms present themselves. When choosing the case of "super-spreaders", the 3rd quartile (also known at 75th percentile) of the distribution is considered, leading to 10^7 virions/mL. By combining the viral concentration, C, with the volume of saliva exiting the mouth, the number of virions in each frame, with a time resolution of 67 µs, is calculated as shown by the yellow curve given in Figure 5a. These data represent the virions contained inside all particles that are positioned and imaged within the 15 mm thick planar illumination. Assuming the "super-spreaders" case, the number of ejected SARS-CoV-2 virions is quantified over time and space, as shown in the accessible movies described below:
- **Movie S3** is an example of high-speed imaging of the number of virions ejected when speaking.
- **Movie S4** is an example of high-speed imaging of the number of virions ejected when yelling.
- **Movie S5** is an example of high-speed imaging of the number of virions ejected when coughing.
The virion flow rate given by the purple curve in Figure 5c differs from all virions in each recorded frame (given by the yellow curve). In this case, only the new particles entering the planar illumination within a temporal duration of 1 ms are considered.

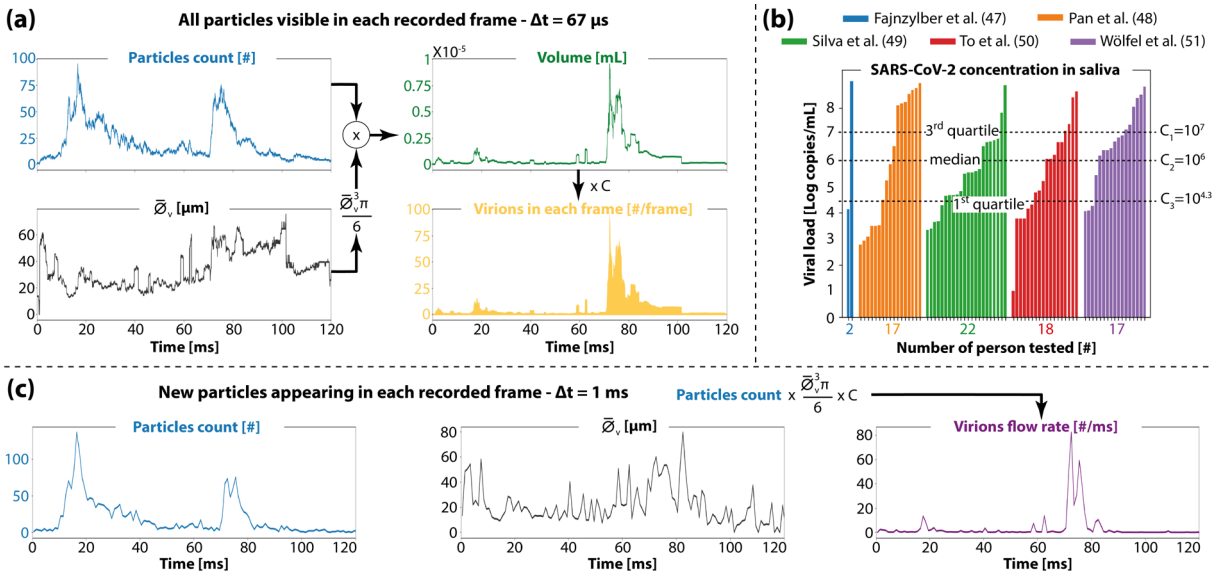

FIGURE 5 Estimation of both the number of virions in each frame and the virions flow rate. (a) shows how the number of virions in each frame is calculated. This is obtained with a time resolution of 67 µs from the measurement of diameter and count over time. The averaged diameter $\bar{\emptyset}_v$ corresponds, here, to the particle diameter calculated from the mean volume obtained during the 67 µs timestep. The number of virions in each frame is deduced by multiplying $\bar{\emptyset}_v$ with the number of particles count and the concentration C of the viral load. (b) is the data from the literature on the viral load contained in the saliva of symptomatic subjects over 5 days. [47-51] Each bar corresponds to one single person. The median and the 3rd quartile are equal to 5.95 and 7.14 log copies/mL viral load, and will be approximated as 10^6 and 10^7 copies/mL respectively. (c) shows how the virions flow rate is obtained by using data after the tracking method. This corresponds to considering the new particles being ejected during a time resolution of 1 ms.

3.2. SARS-CoV-2 virions flow rate when speaking, yelling, and coughing

As mentioned in the previous subsection, the concentration of virions in a patient's saliva changes from day-to-day in accordance with their health. The virion flow rate data presented here assumes a concentration displayed by "super-spreaders" during the first five days of infection, which corresponds to 10^7 virions/mL, as indicated in Figure 5b. Results related to median concentrations of 10^6 or 10^5 virions/mL, can be obtained by simply dividing the presented data by 10 and 100 respectively.
The temporal evolution of particles count (blue lines) and virions flow rate (purple lines) are given for speaking and yelling in **Figure 6**, and for coughing in **Figure 7**. For each cough, the volume flux of each particle size category is shown in **Figure 8**. Those data, are related to the number of particles ejected per millisecond, as described in Figure 5b. The results demonstrate that the emission of virions occurs via a series of successive peaks. This is observed for all scenarios and for each subject. The maximum peaks of virions/ms for speaking, yelling and coughing respectively are: 11.8, 17.6 and 32.7 for Subject #1; 2.8, 5.9 and 20.2 for Subject #2; and 3.7, 5.1 and 27.8 for Subject #3. Those peaks are at the highest when coughing, and vary significantly from one subject to another, with Subject #1 appearing to be the most active spreader. On the right side of Figure 6 and 7, the spatial distribution of the overall liquid volume and number of virions produced during each event are shown on a 2D map. It is observed from those spatial distributions that the cough spreads virions over a much more concentrated area than the speaking and yelling cases. From those images, the differences in spatial particle spreading between the subjects are apparent.

We observe from all results given in Figure 6 that the total liquid volume V_{Tot} given for each event of speaking and yelling, over 1400 ms, are found to be in a range between 0.0028 to 0.021 mm^3. In addition, it is observed that the maximum peaks of particle count do not match with the maximum peaks of virions flow rate. This is explained by the variation in particle size, which directly impacts the total volume of ejected saliva.

The spoken phrase "*Protect better against COVID*", is shown in Figure 6a. The total number of ejected particles are 1311, 1105 and 660; and of ejected virions are 118, 28 and 30, for Subject #1, #2 and #3 respectively. While Subject #1 and #2 emit a similar number of particles, we observe the total number of virions is more than 3 times higher for Subject #1 over #2. This is explained by the presence of a peak of 20 particles with an average diameter $\bar{\emptyset}$ = 29.5 µm, leading to a large volume of saliva ejected by Subject #1. Apart from the presence of only two particles of $\bar{\emptyset}$ = 64 µm, most of those ejected by Subject #2 are smaller than Subject #1, with sizes ranging between 8 and 15 µm. When comparing Subject #2 and #3, a similar total number of virions are ejected but Subject #2 has a total number of saliva particles nearly twice as high as Subject #3. This is explained by the presence of peaks containing droplets with quite large diameters for Subject #3, where $\bar{\emptyset}$ = 53 and 40 µm. As a result, a high number of ejected aerosols, which are more spread out in space, can still remain to an emission of virions lower than the ejection of only a few droplets that are more localized.

When yelling "*Protect better against COVID*", shown in Figure 6b, the total number of ejected particles are 2709, 3080 and 875; and of ejected virions are 207, 68 and 36, for Subject #1, #2 and #3 respectively. In comparison to speaking, it can be seen from Subjects #1 and #2 that nearly three times more particles, and two times more virions, were ejected when yelling. However, for Subject #3, the results have remained equivalent between those two events.
While the number of ejected particles is once again similar between Subject #1 and #2, the total volume V_{Tot} and the number of virions are ~three times lower for Subject #2. This is again explained by the presence of smaller particles ejected by Subject #2, corresponding to aerosols of $\bar{\emptyset}$ =5.6 µm during a maximum peak of 73 particles, which were ejected within 50 ms.

In Figure 7, two coughing events of the three Subjects are shown over 120 ms tracking. the maximum total number of ejected particles per cough is 2911, 684, and 5139 for Subject #1, #2 and #3 respectively. The total liquid volume V_{Tot} given of each event are found to be in a range between 0.0054 to 0.023 mm^3. Compared to speaking and yelling, a cough is a much more "intense" event. This leads to peaks of several hundred particles within only ~10 ms, which is one order-of-magnitude higher than when yelling, and nearly two orders-of-magnitude higher than when speaking. For instance, Subject #3 has the highest particles count peak, which equals 291 particles during Cough 2.

The coughing events are ordered here so that in Cough 1 the size distributions of the ejected particles are more weighted towards the droplets range (20 µm < $\bar{\emptyset}$ < 100 µm) while for Cough 2 the size distributions of the ejected particles are more weighted towards the large aerosols range (5 µm < $\bar{\emptyset}$ < 20 µm). The total liquid volume V_{Tot} ejected over the 120 ms is given for each coughing event on the right side of Figure 7, where a range between 0.0054 to 0.023 mm^3 was found.

Similar to speaking and yelling, the peaks of particles count do not always coincide with the peaks of the virions flow rate, due to the impact of the particle size. The mean particle diameter of the peaks differs significantly over time. For example, during Cough 1 of Subject #1 (Figure 7a) the first peak corresponds to an average diameter of 10.7 µm over 136 particles, while a second peak corresponds to an average diameter of 33 µm over 71 particles. Thus, this second peak gives a virions flow rate of 32.7 virions/ms, which is an order-of-magnitude higher than the first peak, despite having a particles count twice less.
Similarly, in Cough 2 for Subject #2 (Figure 7b), the maximum particles count peak of this event is15 particles with an average diameter of 13.9 µm which gives a virions flow rate of 0.4 virions/ms. However, the presence of only 4 particles of 70 µm mean diameter leads to a much higher virion flow rate reaching 7.6 virions/ms.

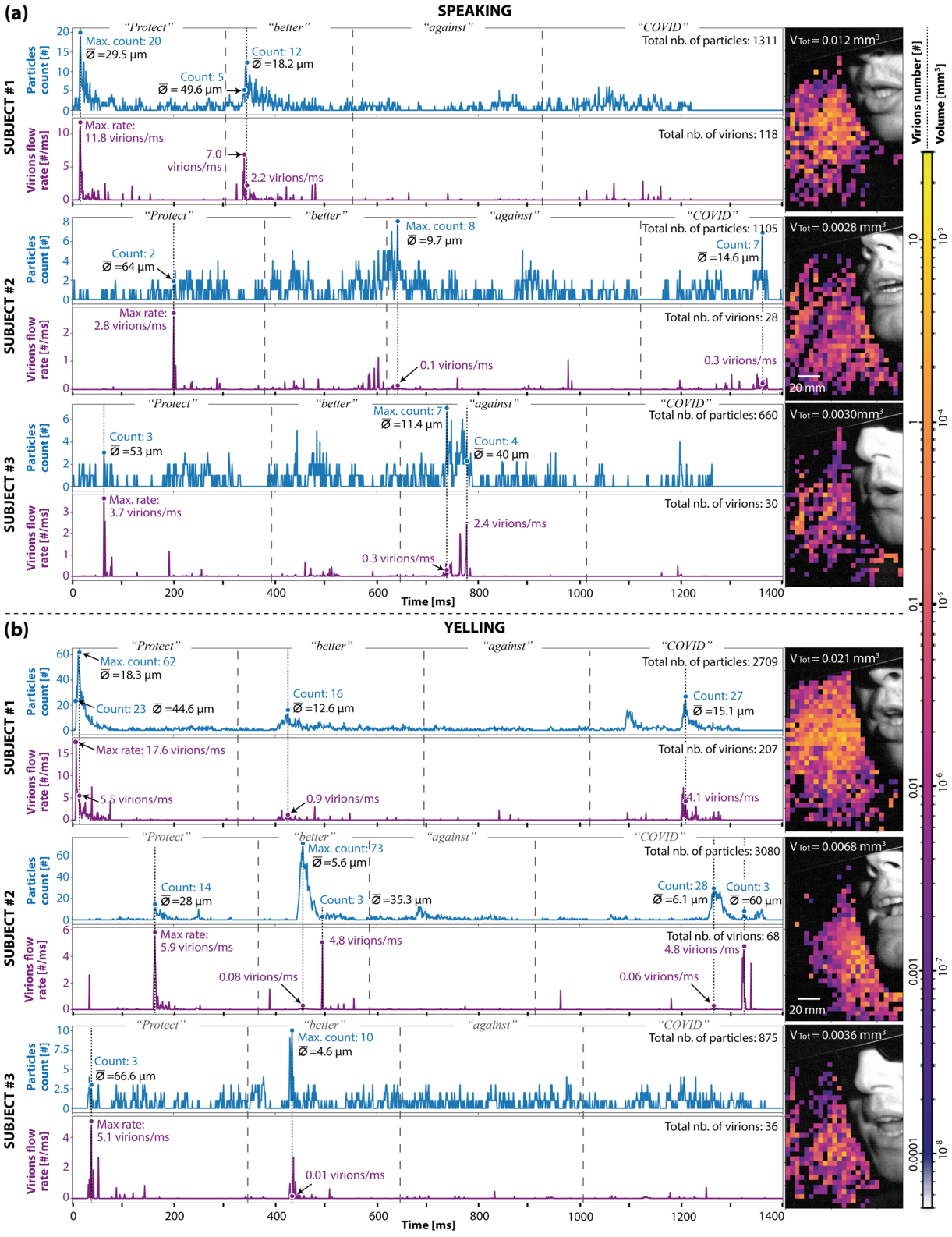

FIGURE 6 Particles count and virions flow rate produced by the three subjects when speaking at ~85 dB (a) and yelling at ~110 dB (b). The data has been deduced quantitatively, as detailed in Figure 5c, assuming a high viral load of 10^7 virions/mL in saliva. The plots are temporally decomposed according to the word spoken, indicated on the top of the plots. The total number of particles and of virions that have been ejected once the sentence is said, are indicated for each case. The spatial distribution of virions is shown on the right side for each event.

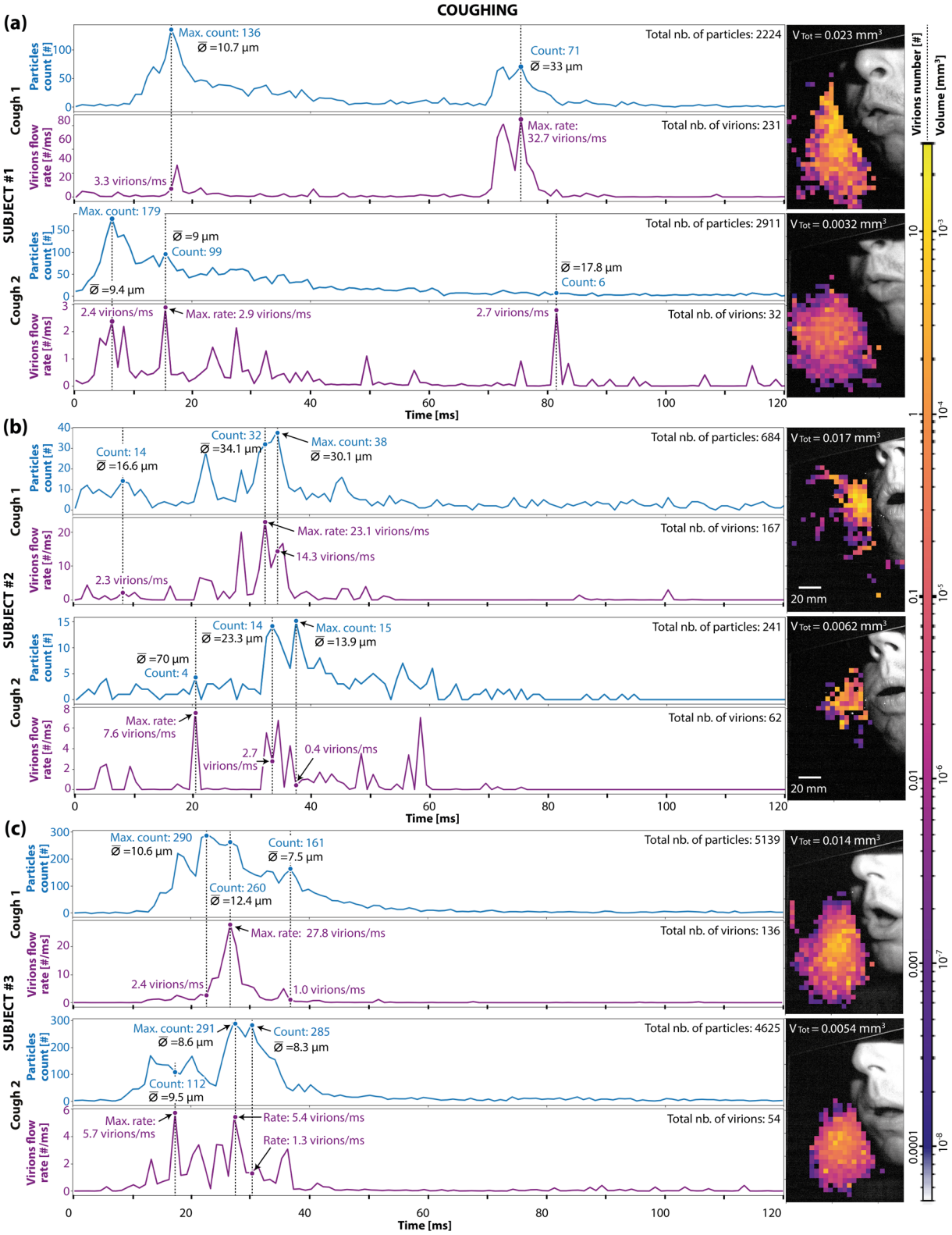

FIGURE 7 Particles count, volume and virions flow rate produced by the three subjects when coughing. The data has been deduced quantitatively, as detailed in Figure 5c, assuming a high viral load of 10^7 virions/mL in saliva. For the cough examples given in (a), the size of the ejected particles belongs more often in the droplets range (20 µm < $\overline{\text{Ø}}$ < 100 µm). For Cough 2 for each subject, the size of the ejected particles belongs more often in the "Large aerosols" range (5 µm < $\overline{\text{Ø}}$ < 20 µm) than in the "Droplets" range (20 µm < $\overline{\text{Ø}}$ < 100 µm). Thus, less virions are being ejected in the Coughs 2 than in Coughs 1. The total number of ejected particles and virions are indicated for each case. The spatial distribution of the virions number, for each event, is shown on the right side.

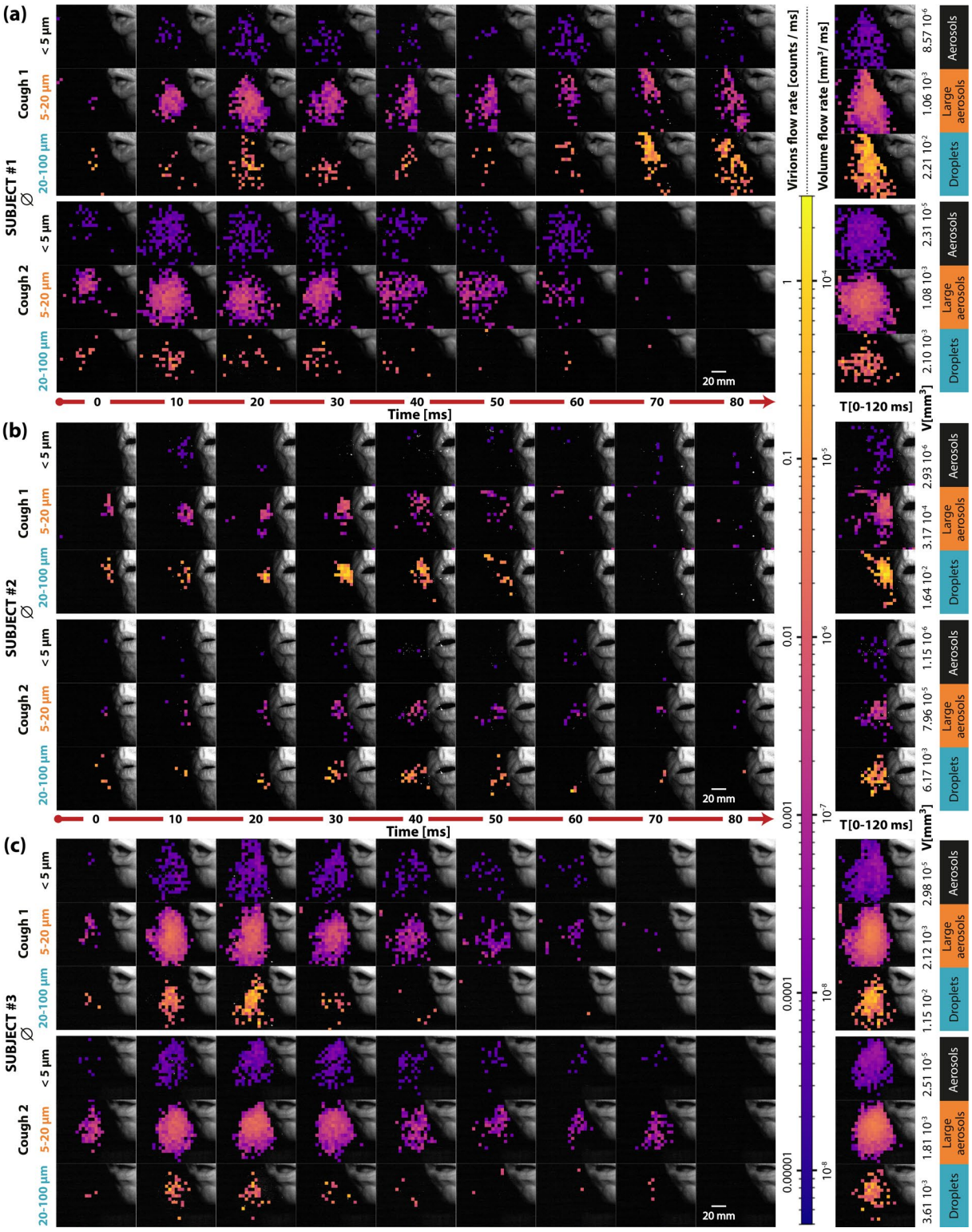

FIGURE 8 Volume and virions flux produced in coughs 1 and 2 for Subject #1 in (a), Subject #2 in (b) and Subject #3 in (c). The flux and flow of each event is subdivided by three particle size categories: the "Aerosols", the "Large aerosols" and the "Droplets". The fluxes are illustrated through time series of frames binned over 10 ms. The volumes and virions flow rate per unit area are given in superpixel space where one unit corresponds to 20x20 pixels or ~16 mm^2. For each particle size category, the accumulated flux and total flow (from 0 to 120 ms) of each event are shown to the right.

The volume and virions fluxes of the coughing events, are given in Figure 8 for three different particle size categories. The temporal decomposition of the flux given in 2D space is shown in time from 0 to 80 ms with a binned frame of 10 ms. Some insights are is given into how the spatial spreading of each particle size category evolves over time. For Subjects #1 and #3, the dominating category in terms of particles count are the "Large aerosols". For Subject #2 there is no dominating size category and only a few "Aerosols" are generated. For all Subjects, the largest total liquid volumes (numbers indicated on the right side of the figure) are found to be for the "Droplets". Then, it is for the "Large aerosols" and finally the "Aerosols". Note that the data from the pictures are given per unit area, where one unit corresponds to the binning of 20x20 pixels or ~16 mm^2. For Subject #2, the spatial spreading is generally smaller than for the other two Subjects.

Determining which range of saliva particles are most likely responsible for the emission of virions requires the knowledge of how many particles have been ejected at each diameter. Large droplets have significantly greater volume but only a small number of them typically occur. Additionally, as shown in Figure 1b, large droplets fall to the ground after traveling a short distance, reducing the probability of their inhalation. Conversely, smaller droplets have the ability to transit a much longer path. Saliva particles ejected with a diameter less than 20 µm, reported here as large aerosols, will rapidly become solid residues smaller than 5 µm in diameter, after the evaporation and efflorescence of the water content. [52] Those particles are then classified as suspended solid aerosols, and can reside in the air for minutes and even hours.[53,54] Luckily, they contain a collectively smaller viral load, and have less protection from the sunlight ultraviolet radiationn.[55]

A crucial question remains: *"Which diameter of ejected saliva droplets is statistically most likely responsible for transmitting the virus, and infecting a new host?"*. Answering this is not trivial, and requires calculating the probability of virus inhalation assuming a given set of conditions. This includes countless parameters such as exhalation velocity, the location of the emitter/receiver, and environmental factors like the temperature and humidity of the surrounding air. The presence of other airflows, such as wind or active ventilation, will also play a role. From the results obtained in this study, we observe that most of the deduced virion flow rate peaks correspond to exhaled saliva particles in the range of 8 to 35 µm diameter; corresponding to the range of large aerosols and small droplets.

4. CONCLUSIONS

An optimized optical setup combined with advanced image post-processing has been developed and applied to provide complete characterization of particle flows produced by human exhalations. This technique offers substantial measurements of aerosols and saliva droplets directly ejected from the mouth, including: a fast data acquisition speed (15 kHz high-speed frame rate), a large interrogation volume (all particles exiting the mouth are illuminated), a high and optimized signal-to-noise ratio (up to 30 times greater detected signal than conventional laser sheet imaging), and a wide sizing range (3.2 - 100 µm diameter). The use of post-processing algorithms has allowed to characterize in detail the aerosols and droplets clouds produced by human subjects. The comprehensive data set includes particle number count, size, speed, and 3D trajectories, all of which are resolved temporally and spatially. In addition, the transition from liquid droplets to solid aerosols has been calculated, using the numerical model described in Ref. [9] to deduce the reduction of particle size after drying a few seconds. As a result, the averaged diameter of the saliva particles, $\bar{\emptyset}$, measured from three subjects, was found to vary between:
- 10.5 and 13.2 µm when speaking, leading to 2.5 to 3 µm solid aerosols after drying,
- 7.5 and 13.4 µm when yelling, leading to 1.7 to 3 µm solid aerosols after drying,
- 9.3 and 15.6 µm when coughing, leading to 2.1 and 3.6 µm solid aerosols after drying.

Thus, no clear trends of particle size distribution separating each exhalation scenario have been observed. However, for the averaged velocity, $\bar{v}$, a trend is noticeable as it varies between 2.4 to 3.4 m/s when speaking, 3.4 to 4.2 m/s when yelling, and, 6.8 and 7.8 m/s when coughing. The maximum speed was reaching over 40 m/s when coughing and yelling.

In addition to the initial velocity measured over the first 15 mm from the mouth, an extended particle tracking over 120 mm has been applied. Those measurements over a longer distance have demonstrated the deceleration of the particles over time and space. We have observed that most saliva droplets of size larger than 20 µm, maintain their initial direction of propagation and reduce exponentially their initial speed. However, most particles of size below 20 µm, are affected by strong varations of their speed and of their direction of propagation. Those effects, which already occur during the first 10 ms, are due to the turbulence of the surrounding airflow. This causes more erratic movements for the small aerosols in comparison to larger saliva particles.
The assumption of the virions concentration of "super-spreaders", has led to the evaluation of the virions flow rates during various exhalations. It has been observed that the saliva particles produced in the size range of 8 to 35 µm and leading to 1.7 to 8 µm sold particles after evaporation, were generating the largest virion flow rates. As a consequence, this may corresponds to the the size range most likely responsible of SARS-CoV-2 airborne transmission.
All results recorded in this study are free to access in Ref. [44] and can be used by modelers as boundary conditions for their simulations. This will enable significant improvements of numerical simulations for deducing the influence of different external parameters. The data provided over the 120 mm distances can also be used to validate the modelling of particles transport and deceleration. By coupling our measurement data with simulations, a better understanding of the spread of virions can be gained. The coupling between the evaporation and the sedimentation of saliva droplets in the air, as well as their virion concentration, will allow to determine the greatest efficiency of virus transmission from one person to another. By applying the methodology of this study to a larger population, definitive answers will be found to questions that continue to surround the transmission of SARS-CoV-2, and other pathogens that spread via airborne pathways. Thus, such work remains paramount in developing effective policies for disease control.

5. EXPERIMENTAL SECTION

5.1. Liquid particles sizing

The procedure for sizing the saliva particles is shown in **Figure 9**. The optical setup used for calibration is shown in Figure 9a, where Cam.1 records shadowgraph images at high-resolution, to resolve the size of the micrometric droplets, and Cam.2 records simultaneously the scattered light intensity over a wide field of view. Thus, this experimental setup combines the recorded intensity of laser light scattering with the corresponding diameter of the illuminated particles.
The amount of light scattered by a spherical micrometric droplet, in the visible spectrum range, is related to its surface area, and thus its diameter. By using the Lorenz-Mie theory,[45,46] the amount of scattered light intensity as a function of the scattering angle, can be calculated for a given particle size. Generating this plot, called the scattering phase function, requires knowing the incident wavelength (λ = 450 nm and 532 nm), the polarization state of the incoming radiation (vertical or horizontal linear polarization), the refractive index of the particle (water is assumed, $n_w = 1.333 - 0.0i$) and the refractive index of the surrounding medium (air is assumed, $n_a = 1.0 - 0.0i$). The scattering phase functions for a droplet diameter of 10 µm and 50 µm, are shown in the top plot of Figure 9b. As observed, the intensity of the scattered light (given in log scale) is much stronger in the forward than in the perpendicular scattering direction. Thus, in this study a semi-forward detection strategy has been used by positioning the cameras in a direction collecting the light scattered between 48° and 56°. The scattering phase function intensity, within this collection angle, is highlighted in the bottom plot of Figure 9b.
The variation of the collected light intensity as a function of particle diameter and collection angle is deduced in Figure 9c. The numerical fit (shown by curves) of those simulated data (shown by crosses) corresponds to the parametric function $\emptyset = a \cdot I_{Mie}^{b}$, where a is a constant in the proportionality between particle area and light scattering and b is near 0.5, since the diameter is related to the square root of the area. It is observed that the optical signal detected around 52° is 30 times higher than a camera collecting around 90°. Consequently, the configuration used in this study allows the detection of much smaller particles.

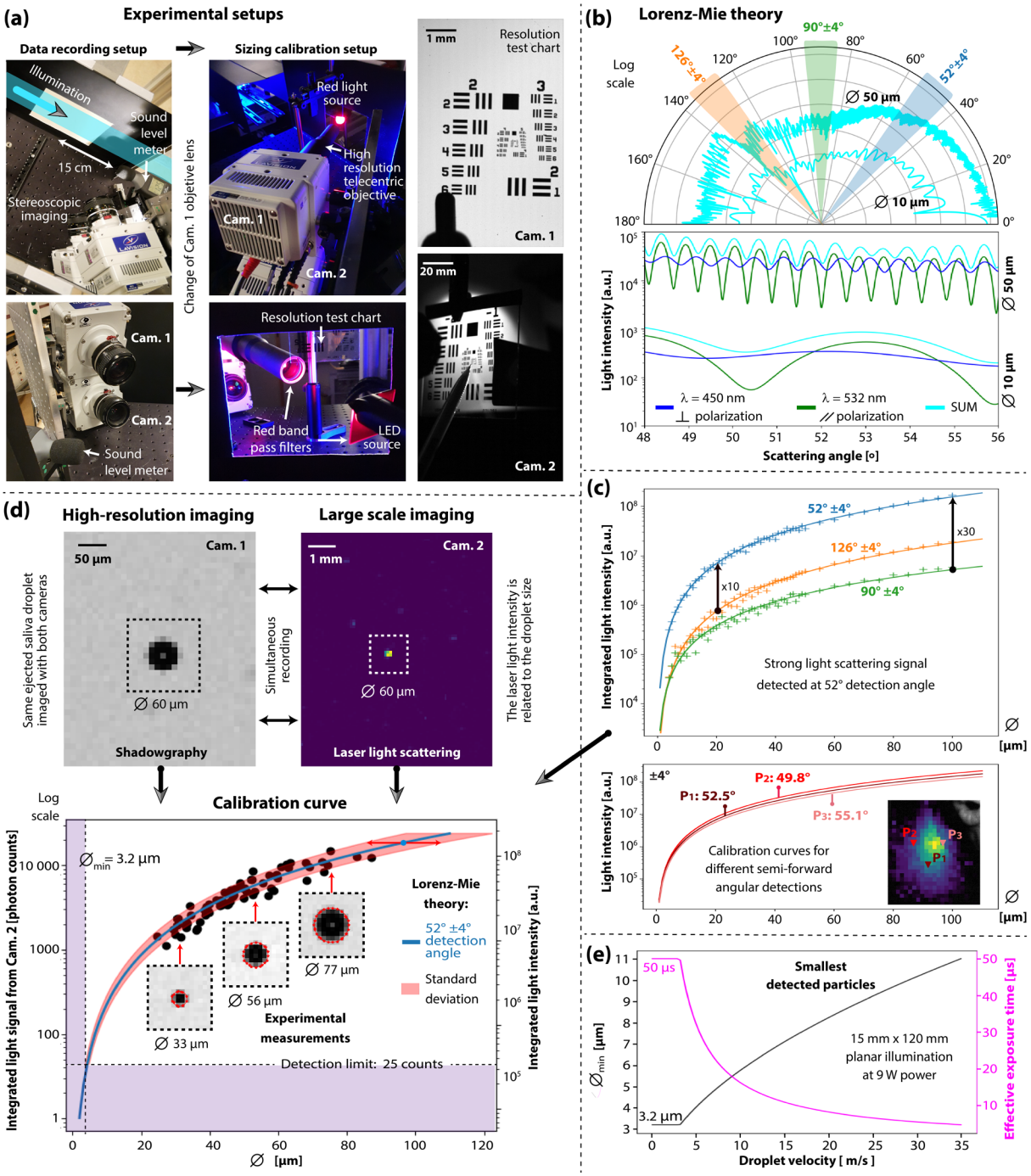

FIGURE 9 (a) Pictures of the experimental setup. The objective lens of Cam. 1 was replaced with a telecentric lens, for directly imaging droplets down to 20 µm. A 1951 USAF target was imaged by both cameras to calibrate the image position. A 640 nm red light source was used to obtain high resolution shadowgraph images in Cam. 1. (b) Using the Lorenz-Mie theory, the upper chart shows the scattering phase functions from the between 0° and 180° for the 10 and 50 µm water droplets. The respective polarizations signals, for the 450 and 532 nm, are summed up to predict the light intensity collected by Cam. 2, at 52° detection. The bottom chart shows the light intensity vs. the droplet size for either 52°, 90° or 126° detection angle. (c) Example of a saliva droplet recorded simultaneously by Cam. 1 and 2. This was repeated for various saliva droplets ranging in between 30 and 70 µm. These data were used to calibrate the curve calculated from the Lorenz-Mie theory. (d) The variation of the calibration curve is shown between three different positions on the recorded images. (e) Calculation of the smallest droplet size measured as a function of droplet velocity. Liquid particles as small as 3.2 µm were detected for the 15 mm thick laser. Droplets traveling at velocity >5 m/s spread their light intensity over several pixels, resulting in lower detection sensitivity.

The detection angle varies slightly as a function of the particle location in space. While 52°±4° is calculated for particles located in the centre of the image, the collection angle changes slightly at other image position. Three examples are given in Figure 9c, demonstrating that those variations do not change significantly the parametric curve.
In Figure 9d, the numerical curve showing the detected light intensity as a function of droplet size is combined with the experimental measurements. This calibration procedure is performed with a person exhaling particles by repeating the letter "v". An example of a 60 µm diameter saliva droplet, simultaneously imaged with the two cameras is shown. A telecentric lens (TC16M018 Bi-telecentric lens from Opto Engineering; 2x magnification) is used with Cam.1, resulting in a spatial resolution of 10 µm/pixel. Shadowgraph images are recorded by applying a background illumination with a bandpass filter in the red region (shown in the pictures given in Figure 9a). This rejects the detection of 450 nm and 532 nm photons by Cam.1, which are instead detected by Cam.2. This second camera collects laser light scattering over a wide field of view using a Nikon objective (Nikkor lens of 35 mm focal and F# 2.8). As the droplets are propagating over a 15 mm wide laser illumination, several successive frames of the scattered laser light are recorded with Cam.2. Thus, the particles are in-focus (stronger maximum signal) when located in the centre of the beam and slightly out-of-focus when located at the edge of the beam (spread of the signal over several pixels). Additionally, as most droplets are displacing at fast speed, the detected scattered light spreads out over several pixels. This effect is detailed in Figure S7 (Supporting Information). Thus, after defining a pixel area where the intensities are above a minimum threshold, a sum of pixel intensities is calculated. This summation gives the value of the detected scattered light (from Cam.2) for a given diameter (measured by Cam.1). This correspondence has been applied for a total of 70 particles, shown in the bottom plot of Figure 9d, to extract a scale of the numerical curve that finalize the calibration procedure. Using a minimum threshold of 25 counts, it is shown that the smallest detectable particle diameter is 3.2 µm. Note that if the illumination used in this study is focused into a 1.5 mm light sheet, the smallest detectable diameter is 1.0 µm (see Figure S8 in Supporting Information).

It is important to note that the minimum detectable diameter is affected by the droplet velocity. This is due to inability of the camera to completely freeze the particle motion (when using 50 µs exposure time), resulting in the captured signal being spread over several pixels, reducing the local pixel intensity (see Figure S7 and S8). This negatively impacts the system ability to capture smaller particles, as the signal falls below the detection limit. For larger particles however, this is advantageous as it avoids saturation. We observe that for the large illumination volume (15 mm), the minimum detectable diameter is 3.2 µm for speeds below 5 m/s and 9 µm at 35 m/s (see Figure S8a). On the other hand, the maximum diameter which is measurable prior to camera saturation increases for the fastest droplets, as the exposure time over a single pixel is reduced by the spread of the signal over several pixels. In this case, it was found that the maximum droplet size that can be measured is 91 µm for speeds below 10 m/s and 250 µm at 35 m/s (see Figure S8b). Those considerations make the effective range of measurable droplet sizes difficult to define since the majority of the droplets measured fall between 3.2 µm and 100 µm.

Figure 9e shows the variation of the minimum detectable size as a function of the particle velocity: For the 15 mm wide laser sheet, the minimum size varies between 3.2 µm and 9 µm for velocity ranging from 0 m/s to 35 m/s. To size the droplets found from a person speaking or coughing, the droplets found in camera Cam.2 are first tracked in 2D pixel coordinates. For each track that is found, the droplet frame with maximum sum intensity is determined and used together with the current image coordinates. Note that two rejection criteria are used for the sizing:

1. If the droplet cannot be tracked for at least 4 frames
2. If any pixel of a droplet is saturated (Less than 1% of the droplets are rejected)

The coordinates are used to extract the current *a* and *b* parameters, and then the diameter is estimated using the parametric equation. The minimum droplet diameter which can be detected using a 15 mm and 1.5 mm thick light sheet are 3.2 µm and 1 µm, respectively. However, the drawback of a thin laser sheet is that it does not allow for an accurate measurement of the droplet diameter, nor does it provide information on the droplet deceleration. It was also found that the 15 mm wide planar illumination was still capturing 94% of the total ejected volume, as demonstrated in Figure S4.

5.1. Liquid particles tracking in 3D

The triangulation procedure for finding the 3D coordinates of the saliva particles is shown in **Figure 10.** The velocity of the exhaled particles is obtained via a post-processing scheme divided into four steps:

1. Find the droplet coordinates in the images of each camera (Figure 10a).
2. Generate the calibration for droplet triangulation (Figure 10b).
3. Triangulate in 3D the droplet positions using the calibration (Figure 10c).
4. Use 3D Particle Tracking Velocimetry (3D-PTV) to calculate droplet paths and velocities.

1. The process of finding coordinates is shown in Figure 10a. Raw images are first scanned for pixels which have been corrupted by unwanted reflections. These are suppressed by way of a mask. A global intensity threshold is then applied to detect and isolate the droplets in the image. All the pixels in camera Cam.1 with a value above 25 counts in the 12-bit images are defined as droplets. The corresponding threshold for Cam.2 is 22 counts since it had lower noise and scattering intensities relative to Cam.1. The image coordinates (x, y) of each droplet are then calculated based on the weighted average of the pixel coordinates and intensities. Having obtained droplet image coordinates from each of the cameras, it is now possible to triangulate the real-world 3D position of each particle using the calibration.

2. The calibration scheme suggested by Machicoane *et al.* in Ref. [56] has been employed, and is illustrated in Figure 10b. In contrast to the classical pinhole camera matrix approach,[57] this method assumes a relationship between each pixel and a line positioned in the 3D global (X, Y, Z) coordinate system. A droplet found in a specific pixel will be positioned in 3D along its corresponding line. To estimate these 3D lines, a known pattern is traversed linearly relative to the cameras. In this work, a checkerboard pattern with 17x10 intersections was employed, as shown in Figure 10b. A total of 13 locations were used, from $Z = 0$ to $Z = 12$ mm.

When the calibration pattern is accurately displaced and imaged, the global X abscissa and Y ordinate remain constant while the Z applicate changes. Thus, for each recorded image the global coordinates of the checkerboard intersections are deduced and their corresponding local image coordinates (x, y) are identified. Using these correspondences, the coefficients of a 2D polynomial transformation L_Z are calculated for each respective Z position. The transform L_Z is then used to convert the local coordinates (x, y) of all pixels of a given image into their global values (X, Y). Due to the linear translation of the pattern, each pixel is associated with 13 points that are aligned in the 3D global coordinate system. By using a total least squares algorithm, a 3D line is estimated for each pixel as shown at the bottom of Figure 10b. The advantage of the approach used here, in contrast with the pinhole approach, is that the optical distortions and properties of the camera are inherently considered.

3. The triangulation process to obtain the 3D coordinates of the droplets is performed from two images recorded simultaneously. The local pixel coordinates (deduced in 1.) of these droplets are denoted x_i^1, x_j^2, while the 3D lines (deduced in 2.) are denoted l_i^1 , l_j^2 for Cam.1 and Cam.2 respectively, where the subscripts i and j are indexes of droplet coordinates. As illustrated in Figure 10c, a crossing of the lines ensures that the same droplet is being identified as a match in between the two images. To find this crossing, the separation distance between two lines is calculated and the smallest one is denoted, d_{ij}. This distance is calculated for all combinations of line pairs. To identify a possible match, the minimum d_{ij} is extracted. If this distance is below a threshold of 200 µm, corresponding to the image pixel resolution, the match is valid and the 3D position of the droplet is set in between the two lines. Finally, those lines are removed in order not to be considered any further. This process is then repeated until the minimum of the remaining calculated distance d_{ij} exceeds the 200 µm threshold.

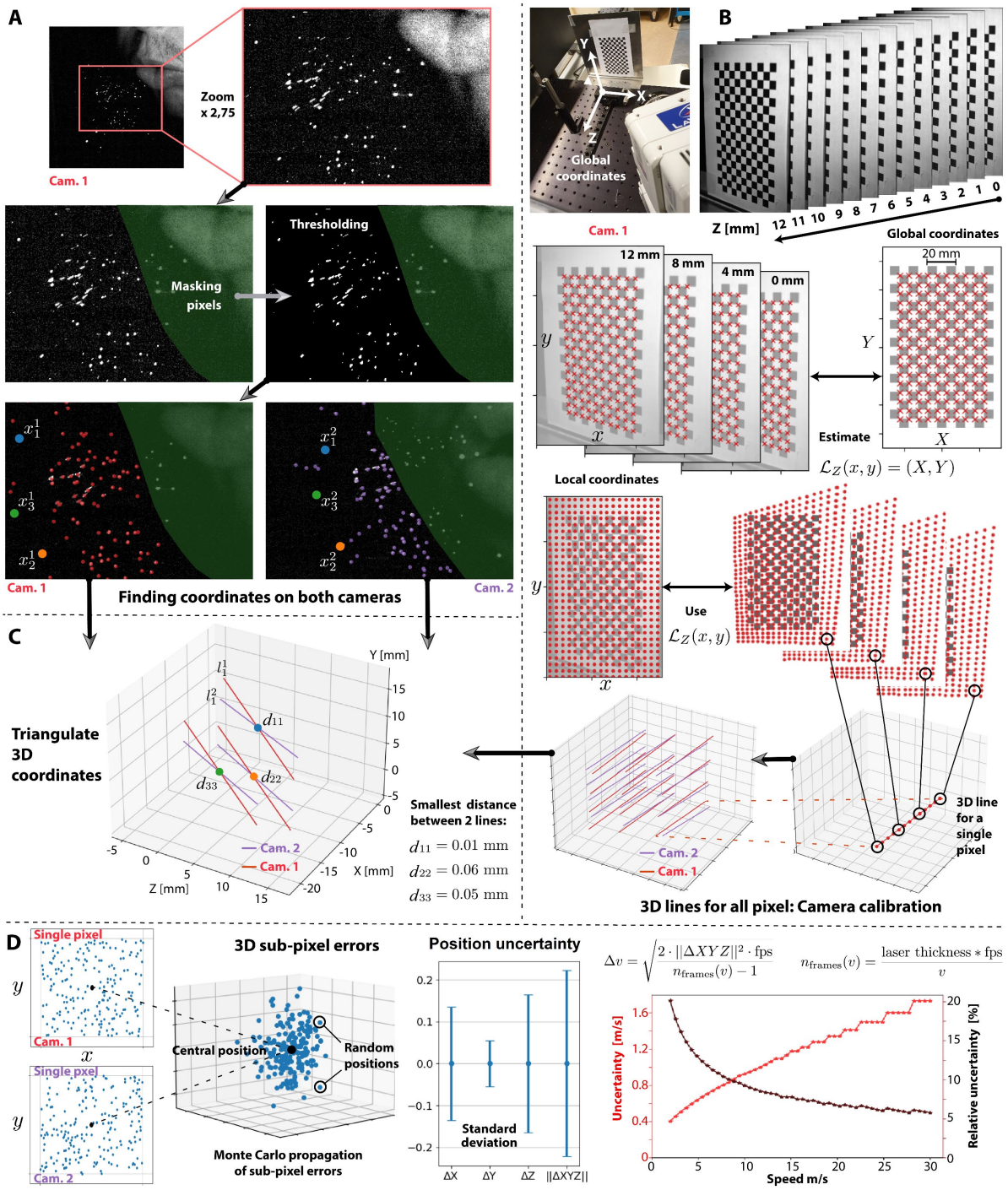

FIGURE 10 (a) Post-processing of the recorded images. The first step is to suppress the light contribution from the person face by applying a mask. The second step consists in suppressing the level of the background. Finally, the coordinates of each droplet are deduced on the images from both cameras. (b) Calibration of the stereoscopic setup. A checkerboard is imaged for the 12 positions along the Z axis. For each position, a $\mathcal{L}$ transformation is estimated to transit from (x, y) local coordinates to (X, Y) global coordinates. Thus, the (XYZ) coordinates, for each pixel, are deduced. Then, the lines along the 12 positions are deduced in 3D. Those lines are shown in red for Cam.1 and in purple for Cam.2. (c) Predicting where the saliva droplets are positioned in 3D requires to find where the lines are crossing each other, a process called triangulation. This position is deduced after finding the smallest distance d between the lines. (d) To estimate the velocity uncertainty from the calibration, a Monte-Carlo approach is used. By generating two random numbers, a specific (x, y) coordinate can be deduced inside a single pixel (+/- 0.5 pixel unit). After obtaining randomized points in one pixel from Cam.1 and one pixel from Cam.2, the global 3D coordinates of a point are deduced by triangulation. This is repeated a large number of times and those random positions are compared, in 3D, with the central position. The standard deviation of those results leads to the position uncertainty $\|\Delta XYZ\|$. The uncertainty of the droplet velocity is then deduced using $\|\Delta XYZ\|$ for a track of the droplet position recorded at 15 kHz.

4. Velocities are calculated using the droplet tracking between frames. The 3D-PTV tracking algorithm developed and used here is inspired by the Four Frame Best Estimate (FFBE) method by Ouelette *et al*. in Ref. [58] and the extension by Clark *et al*. in Ref. [59]. FFBE uses the estimated velocity and acceleration vectors to extrapolate the droplet position in future frames. The droplet which is found to have the minimum distance to this position (denoted here as extrapolation error) is used as the most probable continuation of the track. However, at the initial phase of a track neither the velocity nor acceleration is known. Clark *et al.* suggest trying each combination of droplets in the four future frames, within pre-set limits for the maximum velocity and absolute acceleration. Compared to the FFBE, which uses the nearest neighbor, Clark's approach has been shown to increase the tracking accuracy. We have further developed this recursion to not only include the first four frames, but rather all the frames until the end of the track. A recursive tree is extracted from these results, with all possible droplet paths from an initial position and frame. The tree is limited by predefined maximum velocity, maximum absolute acceleration and a maximum extrapolation error. For each track a score is calculated as the track length subtracted by the sum of all extrapolation errors. The algorithm then selects the track with the best score. In addition, a minimum track length of four is used in order to verify that a track is valid. To quantify how accurate the final 3D coordinates are, an uncertainty analysis has been performed on the camera calibration results (Figure 10d). An error propagation calculation employing a Monte Carlo model was used.

When finding the pixel coordinates of a droplet, the worst-case scenario occurs when in only a single pixel is above the intensity threshold. This results in a pixel coordinate with an integer value. The correct coordinate however, can be anywhere inside the pixel, i.e. ±0.5 pixels. To find the triangulation uncertainty, the difference between the triangulation of correct sub-pixel coordinates, and that of integer coordinates, must be determined. To do so, a set of correct coordinate pairs are sampled from a uniform distribution. They are then triangulated to the correct 3D positions. The same thing is done for the used integer coordinates. The RMS of the error between the correct and used coordinates are then calculated as the uncertainty. For this camera calibration it was found that the uncertainty is approximately 0.2 mm, with the largest uncertainty in the Z-dimension and smallest in the Y-dimension. This can be explained by the camera locations where they are aligned along the world Y-dimension. Note that the uncertainty changes throughout the image between values of 0.16 and 0.22. As shown in the rightmost plot in Figure 10d, the 3D position uncertainty can be used to extract the uncertainty in droplet velocity. The instantaneous velocity of a droplet is calculated by subtracting the 2 positions in different frames, and dividing by the time between frames. This gives an instantaneous velocity uncertainty of $\sqrt{2 \times |\Delta XYZ|^2 \times fps}$ = 1.1 m/s where $|\Delta XYZ|$ = 0.22. The velocity estimations presented here are the averages taken on a number of instantaneous velocity measurements for each droplet. For example, if the droplet is tracked over 8 frames, 7 instantaneous velocity are averaged, lowering the uncertainty. The number of frames will depend on the velocity of the droplet, as shown by the equation in Figure 10d, and results in an uncertainty between 0.4 and 1.6 m/s corresponding to 20% and 5%. Note that these values have been estimated from the worst-case scenarios for droplet identification and position, and thus represent the maximum level of uncertainty.

ACKNOWLEDGEMENTS

This work was conducted at the Department of Physics at Lund University, with the financial support of the Crafoord Foundation grant 20210942, the Swedish Research Council grant 2021-04542 and the Swedish Foundation for Strategic Research grant ITM17-0152.

CONFLICT OF INTEREST STATEMENT

The authors declare no conflict of interests.

DATA AVAILABILITY STATEMENT

All raw images, and results data are openly available and free to download, from Ref. [44]

ETHICS STATEMENT

This work is a non-clinical study which does not requires an official ethical permission from the Swedish Ethical Review Authority. However, an informed consent and agreement from all participants involved in the mesurements was signed.

ORCID

Edouard Berrocal: https://orcid.org/0000-0003-2835-812X

REFERENCES

1. Liu Y, Ning Z, Chen Y, et al. Aerodynamic analysis of SARS-CoV-2 in two Wuhan hospitals. *Nature*. 2020;582:557-560. https://doi.org/10.1038/s41586-020-2271-3
2. Goldman E. Exaggerated risk of transmission of COVID-19 by fomites. *Lancet Infect. Dis.* 2020;20(8):892-893. https://doi.org/10.1016/S1473-3099(20)30561-2
3. Lewis D. COVID-19 rarely spreads through surfaces. So why are we still deep cleaning? *Nature*. 2021;590:26-28. https://doi.org/10.1038/d41586-021-00251-4
4. Morawska L, Tang JW, Bahnfleth W, et al. How can airborne transmission of COVID-19 indoors be minimised? *Environ. Int.* 2020;142:105832. https://doi.org/10.1016/j.envint.2020.105832
5. Jayaweera M, Perera H, Gunawardana B, Manatunge J. Transmission of COVID-19 virus by droplets and aerosols: A critical review on the unresolved dichotomy. *Environ. Res.* 2020;188:109819. https://doi.org/10.1016/j.envres.2020.109819
6. Wells WF, *Am. J. Epidemiol.* 1934;20(3):611-618. https://doi.org/10.1093/oxfordjournals.aje.a118097
7. Lieber C, Melekidis S, Koch R, Bauer H-J. Insights into the evaporation characteristics of saliva droplets and aerosols: Levitation experiments and numerical modeling *J. Aerosol Sci.* 2021;154:105760. https://doi.org/10.1016/j.jaerosci.2021.105760
8. Li H, Leong FY, Xu G, Ge Z, Kang CW, Lim KH. Dispersion of evaporating cough droplets in tropical outdoor environment. *Phys. Fluids*. 2020;32(11):113301. https://doi.org/10.1063/5.0026360
9. Stiti M, Castanet G, Corber A, Alden M, Berrocal E. Transition from saliva droplets to solid aerosols in the context of COVID-19 spreading. *Environ. Res.* 2022;204:112072. https://doi.org/10.1016/j.envres.2021.112072
10. Duguid J. The size and the duration of air-carriage of respiratory droplets and droplet-nuclei. *Epidemiol. Infect.* 1946; 44(6):471-479. https://doi.org/10.1017/S0022172400019288
11. Wang CC, Prather KA, Sznitman J, et al. Airborne transmission of respiratory viruses. *Science*. 2021;373:6558. https://doi.org/10.1126/science.abd9149
12. Bourouiba L. Turbulent gas clouds and respiratory pathogen emissions potential implications for reducing transmission of COVID-19. *JAMA*. 2020; 323(18):1837-1838. https://doi:10.1001/jama.2020.4756
13. Lelieveld J, Helleis F, Borrmann S, et al. Model calculations of aerosol transmission and infection risk of COVID-19 in indoor environments. *Int. J. Environ. Res. Public Health*. 2020;17(21):8114. https://doi.org/10.3390/ijerph17218114
14. Dbouk T, Drikakis D. On coughing and airborne droplet transmission to humans. *Phys. Fluids*. 2020;32(5):053310. https://doi.org/10.1063/5.0011960
15. Feng Y, Marchal T, Sperry T, Yi H. Influence of wind and relative humidity on the social distancing effectiveness to prevent COVID-19 airborne transmission: A numerical study. *J. Aerosol Sci*. 2020;147:105585. https://doi.org/10.1016/j.jaerosci.2020.105585
16. Chaudhuri S, Basu S, Kabi P, Unni VR, Saha A. Modeling the role of respiratory droplets in Covid-19 type pandemics. *Phys. Fluids*. 2020;32(6):063309. https://doi.org/10.1063/5.0015984
17. Armand P, Tâche J. 3D modelling and simulation of the dispersion of droplets and drops carrying the SARS-CoV-2 virus in a railway transport coach. *Sci. Rep*. 2022;12:4025. https://doi.org/10.1038/s41598-022-08067-6
18. Yang S, Lee GWM, Chen CM, Wu CC, Yu KP. The Size and Concentration of Droplets

Generated by Coughing in Human Subjects. *J. Aerosol Med*. 2007;20(4):484-494. https://doi.org/10.1089/jam.2007.0610
19. Morawska L, Johnson GR, Ristovski ZD, et al. Size distribution and sites of origin of droplets expelled from the human respiratory tract during expiratory activities. *J. Aerosol Sci*. 2009;40(3):256-269. https://doi.org/10.1016/j.jaerosci.2008.11.002
20. Asadi S, Wexler AS, Cappa CD, Barreda S, Bouvier NM, Ristenpart WD. Aerosol emission and superemission during human speech increase with voice loudness. *Sci. Rep*. 2019;9:2348. https://doi.org/10.1038/s41598-019-38808-z
21. Sjoeberg H, Manneberg G, Cronhjort A. Long-working-distance microscope used for diesel injection spray imaging. *Opt. Eng.* 1996;35(12):3591-3596. https://doi.org/10.1117/1.601113
22. Glover AR, Skippon SM, Boyle RD. Interferometric laser imaging for droplet sizing: a method for droplet-size measurement in sparse spray systems. *Appl. Opt*. 1995;34:8409-8421. https://doi.org/10.1364/AO.34.008409
23. Querel A, Lemaitre P, Brunel M, Porcheron E, Gréhan G. Real-time global interferometric laser imaging for the droplet sizing (ILIDS) algorithm for airborne research. *Meas. Sci. Technol*. 2010; 21:015306. https://doi.org/10.1088/0957-0233/21/1/015306
24. Chao CYH, Wan MP, Morawska L, et al. Characterization of expiration air jets and droplet size distributions immediately at the mouth opening. *J. Aerosol Sci*. 2009;40(2):122-133. https://doi.org/10.1016/j.jaerosci.2008.10.003
25. Chao CYH, Wan MP. A study of the dispersion of expiratory aerosols in unidirectional downward and ceiling-return type airflows using a multiphase approach. *Indoor Air*. 2006;16:296-312. https://doi.org/10.1111/j.1600-0668.2006.00426.x
26. Bagheri G, Schlenczek O, Turco L, et al. Size, concentration, and origin of human exhaled particles and their dependence on human factors with implications on infection transmission. *J. Aerosol Sci*. 2023;168:106102. https://doi.org/10.1016/j.jaerosci.2022.106102
27. Shao S, Zhou D, He R, Li J, Zou S. Risk assessment of airborne transmission of COVID-19 by asymptomatic individuals under different practical settings. *J. Aerosol Sci*. 2021;151:105661. https://doi.org/10.1016/j.jaerosci.2020.105661
28. Settles GS. *Schlieren and Shadowgraph Techniques: Visualizing Phenomena in Transparent Medi*a , Springer, Heidelberg, Germany 2001. https://doi.org/10.1007/978-3-642-56640-0_6
29. Prasanna Simha P, Mohan Rao PS. Universal trends in human cough airflows at large distances. *Phys. Fluids*. 2020;32(8):081905. https://doi.org/10.1063/5.0021666
30. Tang JW, Nicolle A, Pantelic J, et al. Airflow dynamics of coughing in healthy human volunteers by shadowgraph imaging: An aid to aerosol infection control. *PLoS One*. 2012;7(4):e34818. https://doi.org/10.1371/journal.pone.0034818
31. Tang JW, Liebner TJ, Craven BA, Settles GS. A schlieren optical study of the human cough with and without wearing masks for aerosol infection control. *J. R. Soc. Interface*. 2009;6:S727-S736. https://doi.org/10.1098/rsif.2009.0295.focus
32. Thomann H, Frisk B. Measurement of heat transfer with an infrared camera. *Int. J. Heat Mass Transf*. 1968;11(5):819-822. https://doi.org/10.1016/0017-9310(68)90126-9
33. Koroteeva E, Shagiyanova A. Infrared-based visualization of exhalation flows while wearing protective face masks. *Phys. Fluids*. 2022;34(1):011705. https://doi.org/10.1063/5.0076230
34. Abkarian M, Mendez S, Xue N, Yang F, Stone HA. Speech can produce jet-like transport relevant to asymptomatic spreading of virus. *Proc. Natl. Acad. Sci. U.S.A*. 2020;117(41):25237-25245. https://doi.org/10.1073/pnas.2012156117
35. Bourouiba L, Dehandschoewercker E, Bush JWM. Violent expiratory events: on coughing and sneezing. *J. Fluid Mech*. 2014;745:537-563. https://doi.org/10.1017/jfm.2014.88
36. Bahl P, De Silva C, MacIntyre CR, Bhattacharjee S, Chughtai AA, Doolan C. Flow dynamics of droplets expelled during sneezing. *Phys. Fluids*. 2021;33(11):111901. https://doi.org/10.1063/5.0067609
37. Alsved M, Matamis A, Bohlin R, et al. Exhaled respiratory particles during singing and talking. *Aerosol Sci. Technol.* 2020;54:1245-1248. https://doi.org/10.1080/02786826.2020.1812502
38. Webber BF, Long MB, Chang RK. Two-dimensional average concentration measurements in a jet flow by Raman scattering. *Appl. Phys. Lett.* 1979; 35(2):119-121. https://doi.org/10.1063/1.91042
39. Adrian RJ. Scattering particle characteristics and their effect on pulsed laser measurements of

fluid flow: speckle velocimetry vs particle image velocimetry. *Appl. Opt.*, 1984;23:1690-1691. https://doi.org/10.1364/AO.23.001690

40. Anfinrud P, Stadnytskyi V, Bax CE, Bax A. Visualizing Speech-Generated Oral Fluid Droplets with Laser Light Scattering. *N. Engl. J. Med*. 2020;382:2061-2063. https://doi.org/10.1056/NEJMc2007800
41. Stadnytskyi V, Bax CE, Bax A, Anfinrud P. The airborne lifetime of small speech droplets and their potential importance in SARS-CoV-2 transmission. *Proc. Natl. Acad. Sci. U.S.A.* 2020;117(22):11875-11877. https://doi.org/10.1073/pnas.2006874117
42. Fischer EP, Fischer MC, Grass D, Henrion I, Warren WS, Westman E. Low-cost measurement of face mask efficacy for filtering expelled droplets during speech. *Sci. Adv*. 2020;6(36):eabd3083. https://doi.org/10.1126/sciadv.abd3083
43. Abkarian M, Stone HA. Stretching and break-up of saliva filaments during speech: A route for pathogen aerosolization and its potential mitigation. *Phys. Rev. Fluids*. 2020; 5(10):102301. https://doi.org/10.1103/PhysRevFluids.5.102301
44. Roth A, Stiti M, Frantz D, Corber A, Berrocal E. Exhaled aerosols and saliva droplets measured in time and 3D space: Quantification of pathogens flow rate applied to SARS-CoV-2. *Open Science Framework*. https://doi.org/10.17605/OSF.IO/R7YBD
45. Bohren CF, Huffman DR. *Absorption and scattering of light by small particles*. Wiley, New York, USA 1983.
46. van de Hulst HC, *Light scattering by small particles*, Wiley, New York, USA 1957.
47. Fajnzylber J, Regan J, Coxen K, et al. SARS-CoV-2 viral load is associated with increased disease severity and mortality. *Nat. Commun.* 2020;11:5493. https://doi.org/10.1038/s41467-020-19057-5
48. Pan Y, Zhang D, Yang P, Poon LLM, Wang Q. Viral load of SARS-CoV-2 in clinical samples. *Lancet Infect. Dis*. 2020;20(4):411-412. https://doi.org/10.1016/S1473-3099(20)30113-4
49. Silva J, Lucas C, Sundaram M, et al. Saliva viral load is a dynamic unifying correlate of COVID-19 severity and mortality. *MedRxiv*. 2021. doi.org/10.1101/2021.01.04.21249236
50. To KK-W, Tsang OT-Y, Leung W-S, et al. Temporal profiles of viral load in posterior oropharyngeal saliva samples and serum antibody responses during infection by SARS-CoV-2: an observational cohort study. *Lancet Infect. Dis*. 2020;20(5):565-574. https://doi.org/10.1016/S1473-3099(20)30196-1
51. Wölfel R, Corman VM, Guggemos W, et al. Virological assessment of hospitalized patients with COVID-2019. *Nature*. 2020;581:465-469. https://doi.org/10.1038/s41586-020-2196-x
52. Oswin HP, Haddrell AE, Otero-Fernandez M. The dynamics of SARS-CoV-2 infectivity with changes in aerosol microenvironment, *Proc. Natl. Acad. Sci. U.S.A.* 2022; 119(27):e2200109119. https://doi.org/10.1073/pnas.2200109119
53. Shen Y, Courtney JM, Anfinrud P, Bax A. Hybrid measurement of respiratory aerosol reveals a dominant coarse fraction resulting from speech that remains airborne for minutes, *Proc. Natl. Acad. Sci. U.S.A.* 2022; 119(26):e2203086119. https://doi.org/10.1073/pnas.2200109119
54. Bazant MZ, Bush JW. A guideline to limit indoor airborne transmission of COVID-19, *Proc. Natl. Acad. Sci. U.S.A.* 2021; 118(17):e2018995118. https://doi.org/10.1073/pnas.2018995118
55. Carleton T, Cornetet J, Huybers P, Meng KC, Proctor J, *Proc. Natl. Acad. Sci. U.S.A.* 2020;118(1):e2012370118. https://doi.org/10.1073/pnas.2012370118
56. Machicoane N, Aliseda A, Volk R, Bourgoin M. A simplified and versatile calibration method for multi-camera optical systems in 3D particle imaging. *Rev. Sci. Instrum.* 2019;90(3):035112. https://doi.org/10.1063/1.5080743
57. Tsai RY. A versatile camera calibration technique for high-accuracy 3D machine vision metrology using off-the-shelf TV cameras and lenses. *IEEE J. Robot. Autom.* 1987;3(4):323-344. https://doi.org/10.1109/JRA.1987.1087109
58. Ouellette NT, Xu H, Bodenschatz E. A quantitative study of three-dimensional Lagrangian particle tracking algorithms. *Exp. Fluids*. 2006;40:301-313. https://doi.org/10.1007/s00348-005-0068-7
59. Clark A, MacHicoane N, Aliseda A. A quantitative study of track initialization of the four-frame best estimate algorithm for three-dimensional Lagrangian particle tracking. *Meas. Sci. Technol.* 2019;30:045302. https://doi.org/10.1088/1361-6501/ab0786